In situ root identification through blade penetrometer testing – Part 1

Meijer, Gerrit; Bengough, Anthony; Knappett, Jonathan; Loades, Kenneth; Nicoll, Bruce C. ; Mukov, I; Zhang, M

Published in:
Géotechnique

DOI:
10.1680/jgeot.16.P.203

Publication date:
2018

Document Version
Peer reviewed version

Accepted Manuscript version published in final form in Géotechnique available via:
http://www.icevirtuallibrary.com/toc/jgeot/current

In situ root identification through blade penetrometer testing – Part 1: interpretative models and laboratory testing

G. J. Meijer[*†‡§] A. G. Bengough[*†] J. A. Knappett[*] K. W. Loades[†]
B. C. Nicoll[‡] I. Mukov[*] M. Zhang[*]

Abstract

Root architecture and reinforcement are important parameters to measure the safety of vegetated slopes and stream banks against slope instability and erosion or to assess the stability of plants against environmental loading (e.g. windthrow of trees). However, these are difficult to measure without time-consuming sampling or counting procedures. Previous studies proposed using a penetrometer with an adapted geometry, and showed that individual root breakages could be detected as sudden drops in penetrometer resistance. However, there are no existing models to derive root properties from the measured traces. Here, several interpretative models are developed and their performance at identifying and characterising buried acrylonitrile butadiene styrene (ABS) root analogues of varying diameter and architecture in sand are assessed. It was found that models assuming the analogues broke in bending rather than tension provided good predictions for the force–displacement behaviour. The simple analytical bending model developed here was shown to perform almost as well as more sophisticated numerical models. For all models, the predictions of additional penetrometer force required to break the root analogue were more accurate than predictions for lateral root displacement required to reach failure. The root analogue diameter and to a lesser extent the soil resistance and root angle were shown to affect the penetrometer resistance strongly. Root branching, root length and the distance between the point of load application and a root boundary (root tip or parent root) had a much smaller effect. When the root failure mechanism, root strength, root stiffness and soil resistance are known, an accurate prediction of the root diameter can be made based on the root peak resistance value identified from a blade penetration test. Penetrometer testing, a test which is easy to perform in the field, coupled with an accurate interpretative model might therefore be an effective method to rapidly quantify the spatial distribution, depths and diameters of roots.

1 Introduction

Vegetation can be beneficial for stabilising slopes both through mechanical reinforcement, where roots add strength though tensile or bending action, and hydrological reinforcement, where plants increase soil suctions through water uptake (Coppin and Richards, 1990; Gray and Sotir, 1996; Norris et al., 2008). The mechanical reinforcement added by a single root can be incorporated into existing constitutive soil models as an increase in soil cohesion, often referred to as 'soil cohesion' c_r, following Wu and Waldron's model (WWM, Waldron, 1977; Wu et al., 1979):

$$c_r = k' \cdot \sigma_t \cdot \frac{A_r}{A} \tag{1}$$

[*]University of Dundee, Division of Civil Engineering, Dundee DD1 4HN, UK
[†]James Hutton Institute, Invergowrie, Dundee DD2 5DA, UK
[‡]Forest Research, Northern Research Station, Roslin, Midlothian EH25 9SY, UK
[§]Corresponding author, g.j.z.meijer@dundee.ac.uk

where σ_t is the root tensile strength, A_r the cross-sectional area of the root and A the area of the plane over which the soil strength is determined. A_r/A is commonly referred to as the 'root area ratio' (RAR), i.e. the fraction of the area of a cross-section through the soil occupied by roots. k' is a factor incorporating the effect of the root inclination with respect to the shear plane and the effect of the soil friction angle on the root-reinforcement:

$$k' = \sin\beta + \cos\beta \cdot \tan\phi' \tag{2}$$

where β is the angle between the root axis and the direction perpendicular to the shear plane and ϕ' the soil angle of internal friction. k' is generally assumed as 1.2 (Wu et al., 1979). When this model is used to calculate reinforcement by a bundle of roots, an additional reduction factor k'' is required to take the reduction in reinforcement due to sequential root breakage into account (e.g. Bischetti et al., 2009) and can be determined for example by using a fibre bundle model approach (e.g. Pollen and Simon, 2005; Schwarz et al., 2010). The exact value of k'' depends on root biomechanical characteristics as well as their diameters and quantities. Because of this and because root tensile strength is commonly found to vary with root diameter (Mao et al., 2012), a more accurate expression to calculate root cohesion is:

$$c_r = k' \cdot k'' \cdot \sum_i (\sigma_{t,i} \cdot RAR_i) \tag{3}$$

where the subscript 'i' indicates a single root or root diameter class. Equation 3 indicates that information about both root diameters and root quantity is required to accurately predict mechanical root-reinforcement. This information is also useful when the stability of plants against environmental loading (e.g. windthrow of trees, Nicoll et al., 2006; Achim and Nicoll, 2009) or the effect of roots on the hydrological conditions in the soil is to be modelled, although these applications are outside the main scope of this paper.

Quantifying mechanical root-reinforcement is complicated further by spatial variability in root distributions. Plants adapt to the mechanical, hydrological and chemical conditions within the soil. Soil mechanical impedance limits root growth, and root growth is limited in waterlogged zones (e.g. Stokes et al., 2009; Achat et al., 2008; Nicoll and Ray, 1996). Water and nutrients are distributed heterogeneously throughout the soil, driving preferential root growth. Competition between plants drives changes in root architecture (e.g. Brisson and Reynolds, 1994; Volis and Shani, 2000; Puhe, 2003) and root systems adapt to any aboveground mechanical loading such as wind loading or self weight (Nicoll and Ray, 1996; Stokes et al., 2008) or the effect of growing on slopes (Scippa et al., 2006; Coutts and Nicoll, 1991; Nicoll et al., 2005, 2006). Spatial trends in root distribution are important to consider when quantifying the stability of a slope planted with vegetation since landslides often localise in areas where root quantities are lower (Mao et al., 2014; Moos et al., 2016; Temgoua et al., 2016; Liang and Knappett, 2017).

Since root growth and the resulting architecture depends on many different environmental and genetic factors, it is difficult to acquire good data on the spatial distribution of root properties (e.g. number of roots, root diameter, root depth, lateral spread of roots) without time-consuming invasive excavation techniques. Although the distance to the nearest tree provides some indication of the volume of root material present when combined with aboveground parameters like stem thickness, plant height or canopy volume (Casper et al., 2003; Roering et al., 2003; Schwarz et al., 2010; Docker and Hubble, 2009), input parameters for these root distribution models are site and species dependent, requiring calibration for each case.

Various methods have been used to directly quantify root spatial variability and diameters in situ. Firstly, entire root systems can be excavated. For larger root systems, this can be done by manual excavation (Di Iorio et al., 2005; Henderson et al., 1983b), high pressure water (Watson et al., 1999; Tosi, 2007) or air (Danjon et al., 2008; Stokes et al., 2002) or pulling over whole plants (Nicoll and Ray, 1996; Stokes et al., 2007). Subsequently root architectures can be mapped. However, many roots will be broken or lost during excavation (Danjon et al., 2007; Stokes et al., 2007), especially finer roots, making these methods more useful to study coarse root architecture which may be more resistant to

damage. Root distribution can be measured by counting root intersections on a plane, e.g. the vertical plane of a soil pit (e.g. Abdi et al., 2010; Abernethy and Rutherfurd, 2001; Mao et al., 2012; Pierret et al., 2000; Moos et al., 2016), but this method is labour-intensive and often neglects much fine root material (Bengough et al., 1992). Thirdly, soil cores can be used to sample rooted soil (Ammer and Wagner, 2005; Børja et al., 2008; Danjon et al., 2008; Genet et al., 2008; John et al., 2001; Steele et al., 1997; Wang et al., 2006). After subsequent washing to remove the soil the root biomass can be determined, or roots can be scanned and analysed using image analysis software to extract individual root lengths and diameters. Finally, geophysical methods such as ground penetration radar (GPR) can be applied to locate root depths and spread (e.g. Stokes et al., 2002; Hirano et al., 2009), based on wave reflection of the soil–root interface. A trade-off has to be made between accuracy and root depth making this method more useful to study coarse root architecture. Furthermore, although these methods are non-intrusive, costs are high (Stokes et al., 2002) and accuracy is significantly degraded in soils with high water or clay contents (Hirano et al., 2009).

Because of the limitations of these existing techniques, a new site investigation device that is easy to use *in situ* and negates excavation would be most welcome. Such a device should yield information about the spatial variability as well as the properties of the roots (e.g. root diameter), so this information can be used directly into existing geotechnical root-reinforcement models. Such models could then be used to define the boundaries and properties of zones of enhanced soil properties for finite element simulations and slope stability calculations.

Using an adapted penetrometer ('blade penetrometer') developed by Meijer et al. (2016) for root detection within soils could be such a method. By modifying the penetrometer tip to have a blade-like shape, it was shown that the sensitivity to roots was increased when compared to a standard conical tip. Laboratory testing with various root analogues in low-strength, unsaturated field soil showed that in a fibre-reinforced soil (thin polypropylene fibres) a gradual increase in modified penetrometer force over the rooted depth range could be detected. Thicker root analogues (modelled with acrylonitrile butadiene styrene, ABS) showed distinct reinforcement peaks in the modified penetrometer trace. From the moment the penetrometer hit an ABS root analogue, the resistance gradually increased until the analogue broke, visible as a sudden drop in penetrometer resistance. These peaks of increased resistance will be referred to as 'root peaks', the maximum increase in penetrometer resistance as 'root peak resistance' (F_u) and the corresponding penetrometer displacement from the moment a root is first touched to the moment it breaks as 'root peak displacement' (u_u) in the remainder of this paper. This previous study however gave principally qualitative comparative results; no interpretative model was developed to use the characteristics of these root peaks for root property predictions. In this paper such interpretative methods will be developed and validated against laboratory experiments.

Various interpretative models already exist to predict the behaviour of a single root, for example the Wu/Waldron model introduced earlier for roots crossing a shear plane (Equation 1). The WWM however is not derived to predict the behaviour of a root loaded by a point load (penetrometer tip). It is also not able to predict the shape of the displaced root during loading. A more promising interpretative method is modelling the roots and soil as spring-supported beams. Wu *et al.* (Wu, 2007, 2013) proposed analytical beam models for calculating the root contribution to soil shear resistance, taking into account root bending resistance and axial force, by solving the beam differential equation:

$$E \cdot I \cdot \frac{d^4u(x)}{dx^4} - T_x \cdot \frac{d^2u(x)}{dx^2} = k \cdot d_r \tag{4}$$

where E is the root stiffness, I the second moment of area, x the distance to the shear plane along the root axis, u the lateral root displacement, T_x the axial force in the root in the x-direction, k the linear elastic soil spring resistance (force per unit volume) and d_r the root diameter. Wu et al. (1988) used linear elastic soil springs instead of modelling soil resistance as a constant. However, these initial approaches were not able to take large non-linear displacement effects into account and therefore had to assume that u was small compared to the length of the displaced root. Duckett (2014) and Liang et al. (2015) used non-linear springs in a numerical framework, allowing for non-linear effects and the modelling of large relative root–soil deformations. The properties of these springs were derived from

methods adopted for laterally loaded piles, so called p-y curves (e.g. Randolph and Gourvenec, 2011).

In this study, a new series of laboratory penetrometer tests was performed using buried ABS root analogues with various architectures in dry sand of two differing bulk densities. Two new analytical models for quantitatively assessing root–soil interaction were developed for roots failing in either bending or tension, with various boundary and loading conditions (including blade penetrometer loading and shear loading from displacing soil). Model outputs were validated against a suite of non-linear numerical spring-supported beam models, and empirically against the laboratory test data. All models took both soil and root characteristics into account.

2 Modelling

2.1 Soil resistance to root displacement

The soil resistance acting on laterally displacing roots was estimated using methods derived by Reese and Van Impe (2011) and American Petroleum Institute (2000) for laterally loaded foundation piles. To determine a p-y curve for dry sand, as used in the experiments, both methods require the soil angle of internal friction ϕ', soil unit weight γ', pile diameter d and depth z. In addition, Reese and Van Impe's method requires an additional input value for the spring's initial stiffness. In this work, sands were classified as 'loose' when $\phi' < 30°$, as medium dense when $30° \leq \phi' < 36°$ and as dense when $\phi' \geq 36°$, based on the classification used in the API method (American Petroleum Institute, 2000).

Both methods apply correction factors when curves are determined at shallow depth to account for different soil failure mechanisms such as wedge failure. Because in blade penetrometer tests the root is pushed downwards, vicinity to the surface will not have such a strong influence. Therefore for both methods, when evaluating these correction factors, it was assumed that $z/d = \infty$. Because of this simplification p and y in both methods scale linearly with diameter d, and the ultimate soil resistance p_u as defined by Reese and Van Impe (2011) can be expressed as:

$$p_u = \overline{A}_s \cdot \left(K_a \cdot \gamma' \cdot z \cdot \left(\tan^8 \beta - 1\right) + K_0 \cdot \gamma' \cdot z \cdot \tan \phi' \cdot \tan^4 \beta\right) \tag{5}$$

where $\beta = 45 + \phi'/2$ [°], K_a and K_0 the coefficients of lateral earth pressure in the active case and at rest, and a dimensionless model constant $\overline{A}_s = 0.88$. Example curves for both methods are presented in Figure 1. Both models yielded similar curves when $\phi' \lesssim 40$ but start to diverge at higher values. This is mainly due to some charts in the API method only being usable when $\phi' \leq 40°$. In this analysis, when $\phi' > 40°$ values corresponding with $\phi = 40°$ were used, resulting in underestimation of soil resistance. Because of this limitation, Reese and Van Impe's method was adopted during the remainder of this study.

2.2 Benchmark numerical modelling

Root behaviour under blade penetrometer loading was numerically modelled using Abaqus/Standard version 6.13-1 (Simulia) finite element software. Roots were modelled as one-dimensional beams with non-linear p-y springs attached to account for soil resistance and extra resistance introduced by side branching, see Figure 2a,b,c.

The root material was numerically modelled as linear elastic–perfectly plastic using the maximum root strength as yield stress (Figure 2e). The root itself was implemented in the model using 1-dimensional circular 3-node quadrilateral Timoshenko beam elements to allow for shear strain (Abaqus reference: 'B22'). Non-linear effects of large displacement are taken into account (Abaqus: 'NLGEOM = on'). A soil resistance spring, using p-y curves, was applied to each node (Figure 2d). Because soil p-y curves yield a resistance per unit length, the soil resistance is multiplied by the length of the segment between two nodes projected on to the plane normal to the direction of penetrometer loading (w), see Figure 2b. The penetrometer behaviour was modelled by varying the displacement of the closest node. By step-wise increasing this displacement and analysing residual forces on this node,

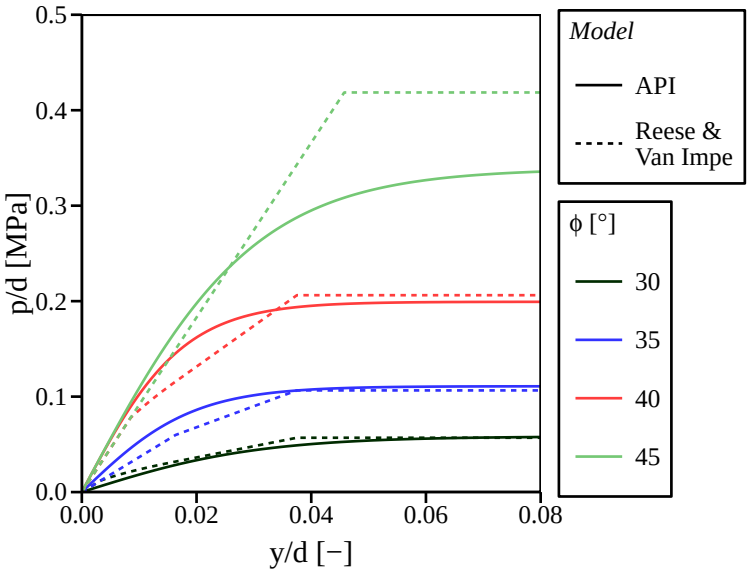

Figure 1: Example p-y curves for piles at 150 mm depth in dry sand generated using methods derived by Reese and Van Impe (2011) and the American Petroleum Institute (2000) (API). p is the lateral soil resistance per unit pile length [Nmm^{-1}] acting on a circular pile with diameter d [mm], while y indicates the lateral pile displacement [mm].

the full force–displacement behaviour of the penetrometer was simulated (Figure 2f). The adopted displacement step size was 0.5 mm. The root was assumed to be broken once the Von Mises stress exceeded the yield stress anywhere in the root.

The friction on the interface between root and soil (τ_i) is difficult to incorporate in a spring-supported beam model, as it depends on many factors, e.g. root type, root tortuosity, root hairs or the presence of mucilage in the rhizosphere. Therefore, two extreme cases were modelled. In the first (Case A), the non-root ends of the soil resistance springs were connected to nodes directly below the root, so the spring force had a component which was active along the axis of root node displacement. Therefore these springs also provide resistance to root axial movement. In this case:

$$\tau_i \approx \frac{p}{\pi} \cdot \cos\beta \tag{6}$$

where p is the soil resistance and β the angle between the root axis and the nodal displacement direction. In the second case (Case B), the soil resistance springs were modelled as very long so that axial deformation does not have any significant influence on the orientation of the spring. Therefore $\tau_i \approx 0$.

The anchoring of a root to a larger parent root or tree stump (the side of the model container in the experiments) was modelled by fixing all degrees of freedom at that end of the root. Root branches were not directly modelled, but represented by additional non-linear springs attached to the modelled 'main' root (Figure 2c). For each branch a force–displacement curve was generated using the same numerical model as used for the 'main' root. The branch was assumed to be broken once the peak strength was reached, after which the branch resistance was set to zero.

2.3 Analytical bending model

The behaviour of roots crossing a shear plane or loaded by a point load (penetrometer) can also be approximated using analytical beam theory (Hibbeler, 2014). Simplifying assumptions made in the modelling, the validity of which will be explored later through comparisons with the numerical models, are:

- The beam/root fails in pure bending. Axial deformations, axial and shear stresses are neglected;

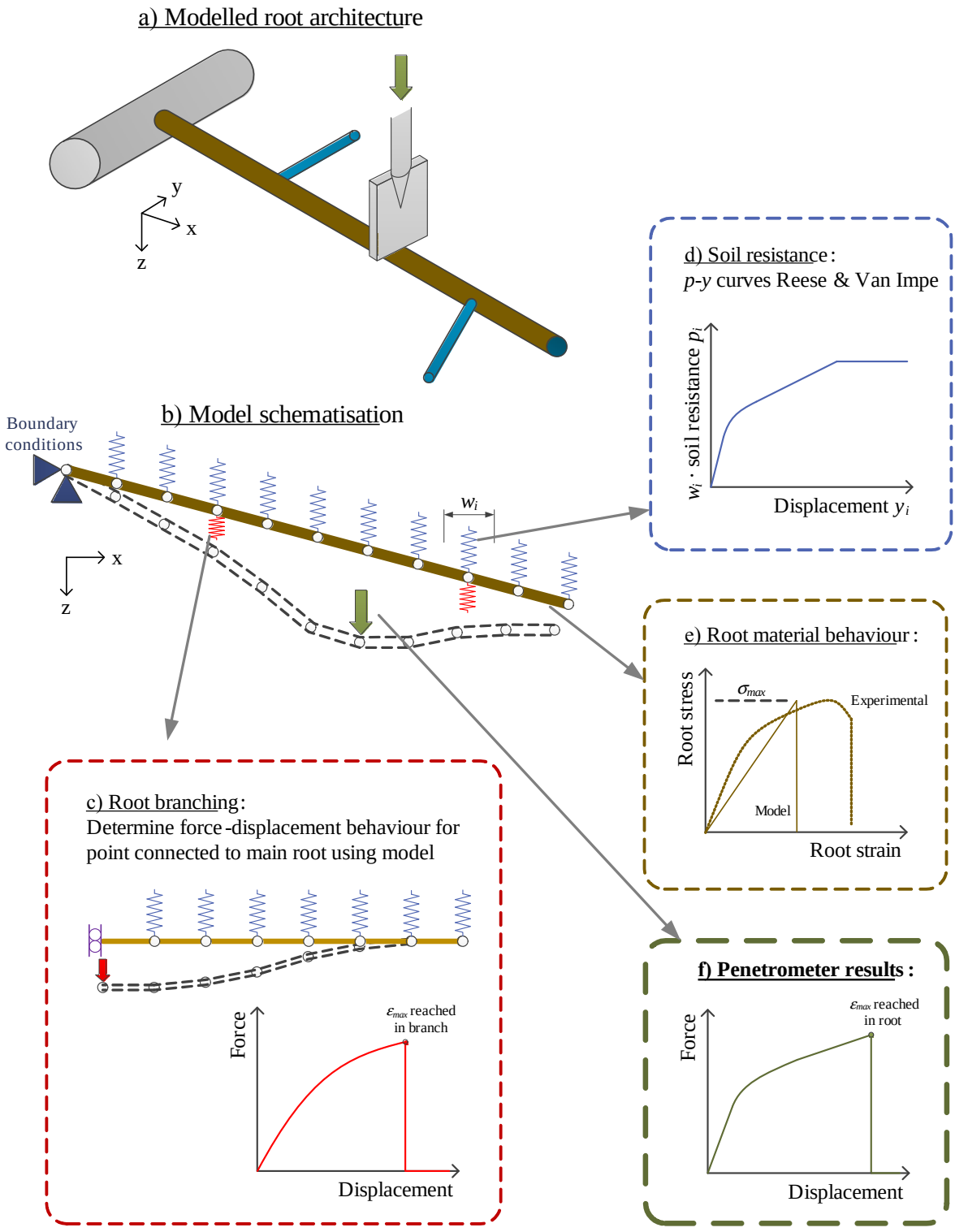

Figure 2: Schematic representation of the numerical modelling procedure. A root with linear-elastic material properties (e) is discretised in small elements (b). To every node a soil resistance spring is attached (d). To some nodes additional springs are attached to model root branching (c). Model results include the penetrometer force and corresponding displacements (f).

- Non-linear geometric effects are neglected;
- Root behaviour is linear elastic up to failure;
- The full soil resistance is mobilised after infinitely small lateral root displacements;
- The root is straight and loaded perpendicular to the root axis.

Under these conditions, the beam displacement can therefore be described using a simplified form of the Euler–Bernoulli differential equation for beam bending:

$$E_b \cdot I \cdot \frac{d^4u(x)}{dx^4} = -d_r \cdot p_u \tag{7}$$

where E_b is the bending stiffness [MPa], u the lateral deformation [mm], x the distance from the point of loading along the beam [mm], p_u is the ultimate soil resistance [Nmm^{-2}] and I the second moment of area, for a circular beam with diameter d_r equal to:

$$I = \frac{1}{64} \cdot \pi \cdot d_r^4 \tag{8}$$

Where the beam is deformed ($|u| > 0$), a constant soil resistance p_u is assumed to be present in the opposite direction to the deformation. Initial numerical simulations indicated the root displacement follows a wave-like pattern, the amplitude of which decreases with increasing distance from the point load. The displaced root shape is therefore simplified as schematised in Figure 3.

This leads to the following boundary conditions for when the beam is vertically loaded in the middle section of the root (Figure 3a):

$$\begin{cases} \frac{\delta u(0)}{\delta x} = 0 & \text{no rotation at point of loading} \\ u(L_1) = 0 & \text{no displacement at } x = L_1 \\ \frac{\delta u(L_{crit})}{\delta x} = 0 & \text{no rotation at } x = L_{crit} \\ u(L_{crit}) = 0 & \text{no displacement at } x = L_{crit} \\ \frac{\delta^3 u(L_{crit})}{\delta x^3} = 0 & \text{no shear force at } x = L_{crit} \\ \frac{1}{2} \cdot F = d_r \cdot p_u \cdot (L_1 - L_2) & \text{vertical load equal to total soil resistance} \end{cases} \tag{9}$$

When the root is loaded at a root end, the following boundary conditions were assumed (Figure 3b):

$$\begin{cases} \frac{\delta^2 u(0)}{\delta x^2} = 0 & \text{no bending moments at } x = 0 \\ u(L_1) = 0 & \text{no displacement at } x = L_1 \\ \frac{\delta u(L_{crit})}{\delta x} = 0 & \text{no rotation at } x = L_{crit} \\ u(L_{crit}) = 0 & \text{no displacement at } x = L_{crit} \\ \frac{\delta^3 u(L_{crit})}{\delta x^3} = 0 & \text{no shear force at } x = L_{crit} \\ F = d_r \cdot p_u \cdot (L_1 - L_2) & \text{vertical load equal to total soil resistance} \end{cases} \tag{10}$$

The same boundary conditions as in Equation 10 apply for roots passing through shear planes within soil. This can be seen as two root end solutions combined (Figure 3c).

Solving Equation 7 once for both $0 \leq x \leq L_1$ and $L_1 \leq x \leq L_{crit}$ with these boundary conditions yields the beam displacement as a function of location on the beam ($u(x)$). The beam is assumed to fail when the maximum bending strength σ_b is exceeded. The maximum bending moment a circular beam can sustain (M_u) is equal to:

$$M_u = \frac{\sigma_b \cdot I}{\frac{1}{2} \cdot d_r} \tag{11}$$

The bending moment can be expressed in terms of beam displacement:

$$M(x) = E_b \cdot I \cdot \frac{\delta^2 u(x)}{\delta x^2} \tag{12}$$

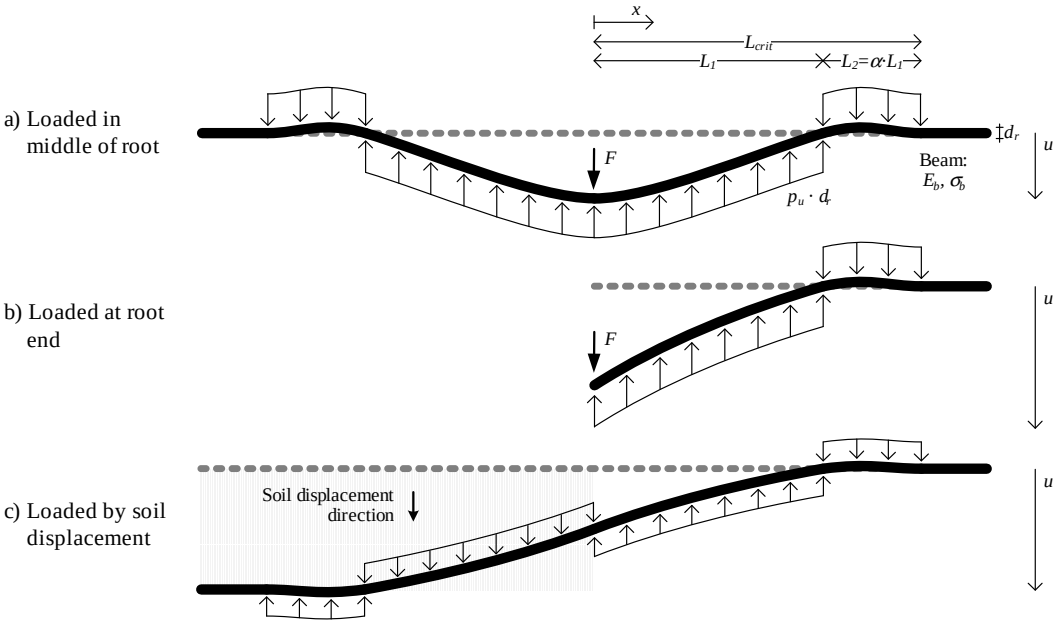

Figure 3: Assumptions and parameters used to solve the analytical beam bending differential equation for different loading conditions: a) infinitely long root loaded by a point load, b) root loaded by a point load at the root end, and c) root loaded by shear displacement of the surrounding soil. The dotted line indicates the original position of the unloaded root. Thin arrows indicate the direction and location of lateral soil resistance (p_u) against root displacement (u).

Table 1: Analytical beam bending solutions. α and L_{crit} are defined in Figure 3. F_u and u_u are the maximum shear of penetrometer resistance (in terms of force) and corresponding displacement associated with beam failure in bending. The maximum root stress is reached first at $x = x_u$. The force–displacement behaviour of the point load or shearing soil is given by $u(F)$.

	Formula			Multiplication factor
	Penetrometer		Shear plane	
	Middle of root	Root end		
α	0.2695	0.4248	0.4248	
L_{crit}	0.8311 ξ_1	1.0976 ξ_1	1.0976 ξ_1	$\xi_1 = d_r \cdot \sigma_b^{0.5} \cdot p_u^{-0.5}$
F_u	1.0231 ξ_2	0.4431 ξ_2	0.8862 ξ_2	$\xi_2 = d_r^2 \cdot \sigma_b^{0.5} \cdot p_u^{0.5}$
u_u	0.09808 ξ_3	0.5247 ξ_3	1.0493 ξ_3	$\xi_3 = d_r \cdot \sigma_b^2 \cdot E_b^{-1} \cdot p_u^{-1}$
x_u	0	0.4431 ξ_4	0.4431 ξ_4	$\xi_4 = d_r \cdot \sigma_b^{0.5} \cdot p_u^{-0.5}$
$u(F)$	0.08954 ξ_5	13.61 ξ_5	1.7011 ξ_5	$\xi_5 = F^4 \cdot d_r^{-7} \cdot E_b^{-1} \cdot p_u^{-3}$

Using Equations 11 and 12, both the location where bending stresses will be highest and the magnitude can be found. Thus the beam deformations associated with failure in bending can be obtained.

Results for the critical length (L_{crit}), root peak resistance (F_u) and root peak displacement (u_u) associated with beam failure in bending, the location of bending failure (x_u) and the penetrometer or soil displacement associated with penetrometer or shear resistance $u(F)$ are summarised in Table 1. In the case of roots loaded by shearing soil, F_u is defined as the maximum root contribution to the shear resistance. The length of root which displaces as an effect of the applied load (L_{crit}) increases with diameter and bending strength, and diminishes with increased soil resistance. The root peak resistance corresponding with bending failure (F_u) goes up with increasing bending strength, increasing soil resistance and especially with increasing diameter. The root peak displacement (u_u) increases when bending strength and diameter are increased, and decreases when bending stiffness and soil resistance are increased.

2.4 Analytical cable model

An alternative mechanism by which the root may add additional penetrometer resistance is through tensile action. This may be more likely to occur than bending for roots with low $E \cdot I$, under which conditions lateral relative soil–root deformations will be large. Existing tension-based models which consider roots to act as rods (i.e. neglecting lateral displacements) may be insufficient to capture such behaviour and so an analytical model was developed assuming roots behave as buried laterally flexible cable elements loaded in tension. The effects of root axial strain are incorporated in this model.

This modelling approach assumes that:

- The cable fails in pure tension;
- The cable can only support axial tension forces. Compression, bending and shear forces and stiffnesses were neglected;
- The cable behaviour is linear elastic with axial stiffness E_t;
- The full soil resistance is mobilized after infinitely small lateral root displacements (as with the bending model);
- The cable is straight and loaded perpendicular to the cable axis.

The force a horizontal cable, vertically loaded by a point load, can sustain in tension can be estimated using force vector decomposition once the maximum angle between the deformed root under the penetrometer tip and the horizontal axis (β, see Figure 4) is known:

$$F_u = 2 \cdot F_t \cdot \sin(\beta) \tag{13}$$

where the factor 2 originates from tensile loading to both sides of the penetrometer and where F_t is the root tensile force at failure, equal to:

$$F_t = \frac{\pi}{4} \cdot d_r^2 \cdot \sigma_t \tag{14}$$

where σ_t is the root tensile strength. However, β depends on the root–soil interaction and is therefore not known a priori.

A solution for β was found using analytical modelling. Only half of the root was modelled because of symmetry. At the penetrometer location, horizontal deformations were assumed to be restrained and at the other end of the root both vertical and horizontal displacement were fixed to zero, see Figure 4. The half-cable is split into two zones. In zone I, closest to the penetrometer tip, vertical soil resistance is mobilised. Since this is the only force counteracting the penetrometer force, the length of this zone can be expressed as:

$$L_I = \frac{1}{2} \cdot \frac{F_u}{p_u \cdot d_r} \tag{15}$$

Over the length of zone II, it is assumed that the root only strains in the axial direction and no lateral soil resistance is mobilised. The length of this zone is equal to:

$$L_{II} = L - L_I \tag{16}$$

The horizontal component of the cable axial force is constant over the whole cable length since all external forces act vertically. Therefore, the maximum axial force will occur where the root deformation angle is largest, i.e. under the penetrometer tip. Equation 13 described this maximum angle. The maximum axial stress in zone II can then be expressed as:

$$\sigma_{II} = \sigma_t \cdot \cos\beta \tag{17}$$

The increase in length due to this axial stress is:

$$\Delta L_{II} = \frac{\sigma_{II}}{E_t} \cdot L_{II} \tag{18}$$

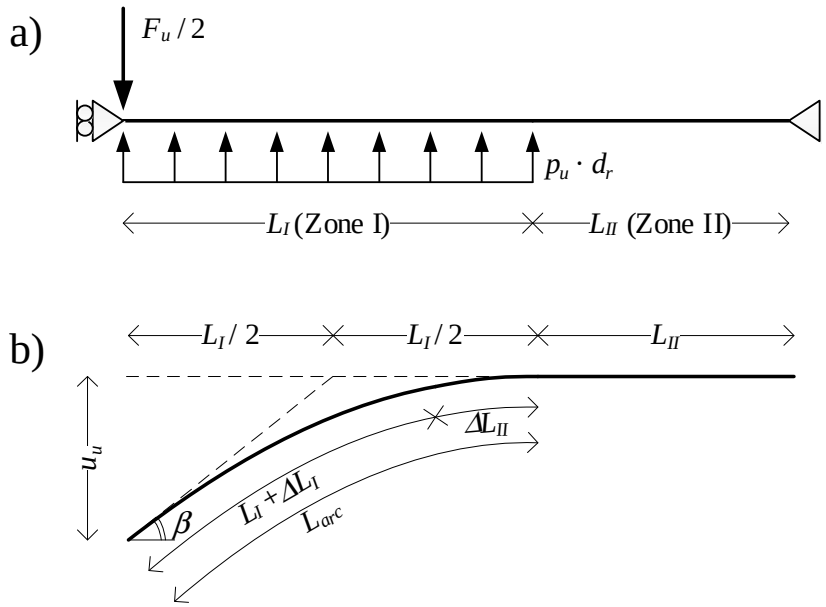

Figure 4: Schematic analytical cable model. a) schematic loading and boundary conditions, b) schematic cable deformation. The external point load (F_u) is counteracted by lateral soil resistance (p_u) over a length L_I. As a result, the cable displaces both laterally and axially in zone I, but only axially in zone II. Because of symmetry, only half the root is shown.

The deformations in zone I were more difficult to model due to non-linear effects, and were estimated as follows. Since the root is modelled as a cable and the soil resistance is constant over length L_I, the cable will deform in a parabolic shape. The length of this parabolic section can be estimated using the analytical solution for parabola arc length:

$$L_{arc} = \sqrt{\frac{L_I^2}{4} + u_u^2} + \frac{L_I^2}{4 \cdot u_u} \cdot \sinh^{-1}\left(\frac{2 \cdot u_u}{L_I}\right) \tag{19}$$

where u_u is the vertical deformation under the penetrometer tip. This parameter can be estimated in turn using another property of a parabola, stating that the maximum gradient is equal to twice the average gradient:

$$u_u = \frac{L_I}{2} \cdot \tan\beta \tag{20}$$

The average stress in zone I (σ_I) is estimated by averaging the stress at the beginning and end points of the parabola:

$$\sigma_I = \frac{1}{2} \cdot (\sigma_t + \sigma_{II}) \tag{21}$$

and the increase in length is then:

$$\Delta L_I = \frac{\sigma_I}{E_t} \cdot L_I \tag{22}$$

Now two different derivations to predict the length of the deformed root have been obtained: one through root axial deformation under root stress and one through the arc length of the deforming root. Both predictions should give similar results, so:

$$L_{arc} \approx L_I + \Delta L_I + \Delta L_{II} \tag{23}$$

All parameters in Equation 23 can be expressed in terms of root (d_r, σ_t, E_t and L) and soil characteristics (p_u), along with the penetrometer force at root tensile failure F_u.

There is no closed-form solution for Equation 23 rewritten in terms of F_u. Therefore, the equation was numerically solved for every combination of a large number of parameters: $d_r \in \{0.5, 1, 2, 4, 8\}$ [mm], $\sigma_t \in \{5, 10, 20, 50, 100\}$ [MPa], $E_t \in \{50, 100, 200, 500, 1000\}$ [MPa], $L \in \{10, 20, 50, 100, 200, 500, 1000\}$

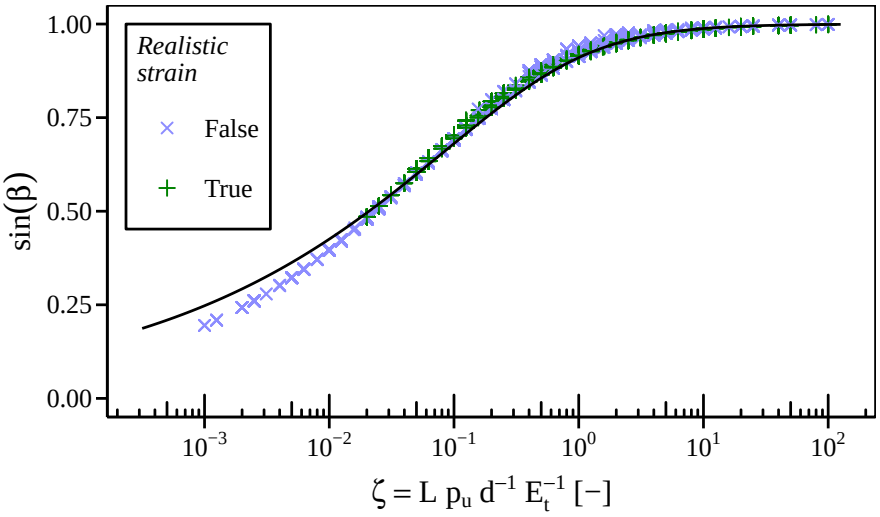

Figure 5: Analytical cable model solutions for the maximum angle between deformed and undeformed cable. Realistic strain values are defined as $0.05 \leq \sigma_t \ E_t^{-1} \leq 0.20$ (Coutts, 1983; Operstein and Frydman, 2000; Schmidt et al., 2001).

[mm] and $p_u \in \{0.1, 0.2, 0.5, 1, 2, 5\}$ [MPa], totalling 4375 combinations. The range of root diameters (d_r) was chosen to reflect diameters that realistically could be broken with the device. Root mechanical properties (σ_t, E_t) cover the tensile strength and stiffness range of roots with diameters $1 \leq d_r \leq 10$ mm reported in literature (Mao et al., 2012; Liang et al., 2015; Meijer et al., 2016). As roots are known to elongate slowly penetrating into soil with penetrometer resistances exceeding $q_c = 2$ MPa (Bengough and Mullins, 1990; Stokes et al., 2009), the range of p_u is chosen accordingly. Root length L is the largest unknown, and therefore a wide range of values was selected, spanning two orders of magnitude.

The results (Figure 5) show that the angle between the cable and the horizontal increases with increasing root length and soil resistance and with decreasing cable diameter and tensile stiffness. The results for β were fitted in the following form:

$$\tan\left(\frac{\beta}{2}\right) = \sqrt{\eta} \tag{24}$$

where:

$$\eta = \sqrt{\frac{\zeta - 2 \cdot \sqrt{\zeta + 1} + 2}{\zeta}} \tag{25}$$

$$\zeta = \frac{L \cdot p_u}{d_r \cdot E_t} \tag{26}$$

This shape ensures that the solution yields realistic values at extreme values of ζ. β approaches 0 at low values of this parameter (no root deformation) and $\pi/2$ at high values (root oriented almost vertically under the penetrometer tip). Using Equations 14, 15, 20 and 24, the root peak displacement at failure simplifies to:

$$u_u = \frac{\pi}{4} \cdot d_r \cdot \frac{\sigma_t}{p_u} \cdot \sqrt{\zeta} \tag{27}$$

and the root peak resistance to:

$$F_u = \frac{\pi}{4} \cdot d_r^2 \cdot \sigma_t \cdot \frac{4 \cdot \sqrt{\eta}}{1 + \eta} \tag{28}$$

In reality, there will be a component of friction between the root and the surrounding soil (τ_i), affecting axial strains and therefore influencing the cable deformation. Since the fixed model boundary at $x = L$ has a similar effect in this model, one was expressed in terms of the other. Assumptions

were that the total cable elongation in both cases was equal. The maximum friction force is assumed to be equal to the tensile force corresponding with failure. τ_i was assumed to be constant over the length of the cable, so the axial force decreases linearly with x and reached 0 at a distance:

$$L_\tau \approx \frac{F_t}{\pi \cdot d_r \cdot \tau_i} = \frac{d_r \cdot \sigma_t}{4 \cdot \tau_i} \tag{29}$$

The total axial increase in length of the cable is then equal to

$$\Delta u_{x,1} = \frac{1}{2} \cdot L_\tau \cdot \frac{\sigma_t}{E_t} \approx \frac{d_r \cdot \sigma_t^2}{8 \cdot \tau_i \cdot E_t} \tag{30}$$

The corresponding model length L can be found when $\Delta u_{x,1}$ is compared with the increase in cable length ($\Delta u_{x,2}$) computed using the cable stiffness and stress in the cable:

$$\Delta u_{x,2} \approx L \cdot \frac{\sigma_t}{E_t} \tag{31}$$

Solving $\Delta u_{x,1} = \Delta u_{x,2}$ results in:

$$L \approx \frac{d \cdot \sigma_t}{8 \cdot \tau_i} \tag{32}$$

Therefore, using Equation 26:

$$\zeta \approx \frac{\sigma_t \cdot p_u}{8 \cdot E_t \cdot \tau_i} \tag{33}$$

Equation 33 can then be used instead of Equation 26 to find ζ, from which η can be found from Equation 25 and then F_u and u_u from Equations 28 and 27 respectively.

The cable model can also easily be used to calculate the reinforcement a single root perpendicularly crossing a shear plane adds to soil. Because of symmetry, the force required to fail a root due to shearing soil will be half that of the penetrometer force, and the soil displacement twice that of the penetrometer displacement. The multiplication factor in Wu and Waldron's original root-reinforcement model (Equation 1), accounting for the effect of soil friction angle and the angle between root and shear plane, can then be expressed in terms of the analytical cable model as:

$$k' = \sin\beta + \cos\beta \cdot \tan\phi' = \frac{2 \cdot \sqrt{\eta}}{1+\eta} + \frac{1-\eta}{1+\eta} \cdot \tan\phi' \tag{34}$$

Equation 34 shows that the root peak contribution to soil shear strength through tensile action is not only a function of root diameter, tensile strength and soil angle of internal friction, but also of soil–root interface friction, root tensile stiffness and soil resistance. Depending on the exact values of ϕ' and ζ, the contribution of a single root to shear strength might be smaller or larger compared to the Wu/Waldron model (Figure 6). An additional advantage over the Wu/Waldron model is that the analytical cable model provides insight into the root displacements required to reach tensile failure, which are shown to increase with increasing root diameter and strength, and decreasing soil resistance and root stiffness.

3 Laboratory experiments

Many laboratory blade penetrometer tests were performed to verify the numerical and analytical models using dry sand and buried ABS root analogues. Various soil densities (50% and 80% relative density) and root properties (diameter, architecture) were tested.

3.1 Root analogues

Acrylonitrile Butadiene Styrene (ABS) plastic was selected as root analogue material. This material has comparable mechanical characteristics to plant roots (Liang et al., 2014, 2015; Meijer et al., 2016). A rapid prototyper ('3D-printer') was used to print roots in various configurations. ABS strength and

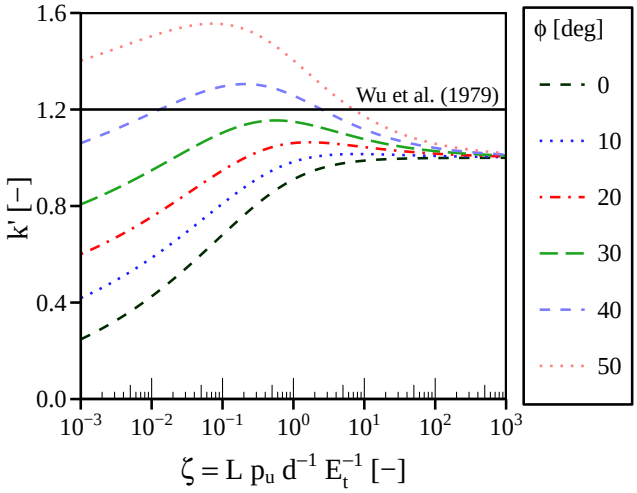

Figure 6: Comparison between the analytical cable model and Wu/Waldron model (Wu et al., 1979). ϕ indicates the soil angle of internal friction

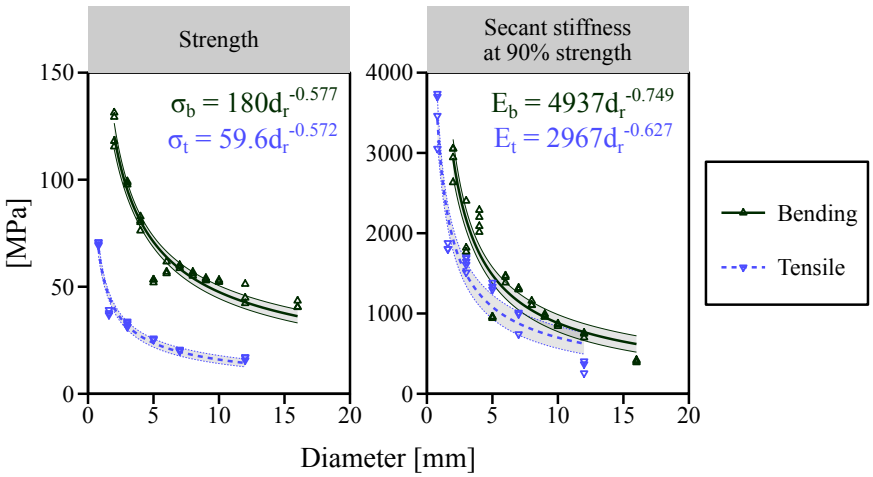

Figure 7: Tensile and bending strength and stiffness of printed Acrylonitrile Butadiene Styrene (ABS) plastic. Data obtained from testing by Liang et al. (2015). Lines indicate best power law fits and shading the 95% confidence interval of these fits.

stiffness was measured in both tension and bending using a universal testing machine by Liang et al. (2015) (Figure 7). The secant stiffness at 90% of the peak strength (E_{90}) was determined from stress–strain curves. E_{90} was chosen due to yielding a better approximation of the non-linear stress–strain curve when using a linear elastic material model.

Root analogue diameters were 2 and 4 mm with lengths of 200 or 400 mm. Because of the limited print volume of the 3D-printer, 400 mm rods were made by connecting two 200 mm rods with epoxy resin and a printed ABS coupler with a length of 15 mm and an external diameter 3 mm larger than that of the rod. Roots with three commonly modelled architectures were tested: unbranched, herringbone branching and perpendicular branching (Figure 8) (Dupuy et al., 2005a; Hamza et al., 2007; Mickovski et al., 2007). The adopted branching angle for the herringbone pattern was 45°, similar to values found *in situ* (Henderson et al., 1983a; Riestenberg, 1994). Branch length was chosen as 60 mm and branching distance as 200 mm (herringbone) or 100 mm (perpendicular), close to the 150 mm reported for d_r = 1–5 mm Norway spruce (*Picea abies*) roots (Giadrossich et al., 2013). All tested 2 mm diameter roots were unbranched. Branch diameter was 2 mm, so that the

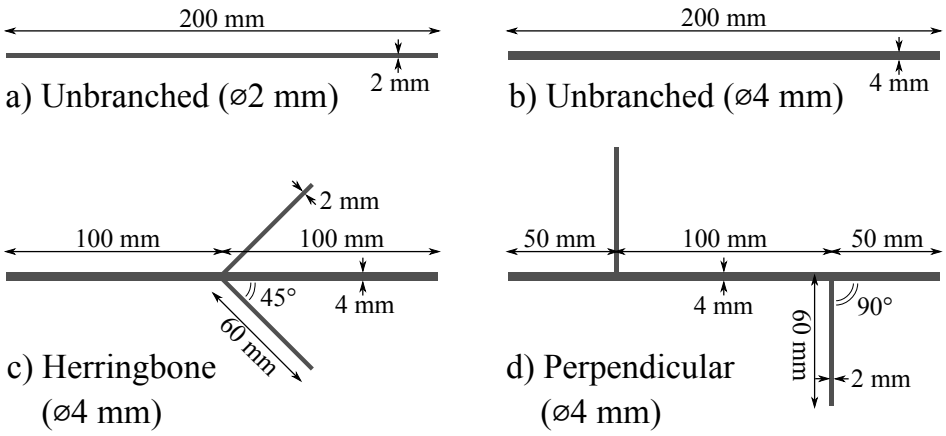

Figure 8: Root architectures and branching patterns for 200 mm long analogue root sections.

child–parent diameter ratio in branched cases was 0.5, similar to the 0.45 used by Dupuy et al. (2005b) for Maritime pine.

All tests were performed at a root depth $z = 150$ mm. One root end was securely anchored to the side of the model container to simulate the root being connected to a larger parent root. Roots were oriented in the horizontal plane or at an angle to the horizontal ('inclined root', 30° dipping down). 400 mm long horizontal root analogues were loaded at either 100 or 300 mm distance from the 'parent root' (measured along the root axis) while 200 mm long horizontal analogues were loaded only at 100 mm distance. Inclined roots were only loaded at 300 mm (400 mm long roots) or 100 mm distance (200 mm long roots) from the 'parent root'. All inclined roots tested were unbranched.

3.2 Soil and sample preparation

Dry Congleton silica sand (HST95) was used as soil. Tests were performed in medium dense (relative density $I_d = 50\%$) and dense sand ($I_d = 80\%$). The relative density indicates the density on a scale from 0% (loosest achievable density) to 100% (highest achievable density).

From previous experimentation the following correlations were derived for soil peak angle of internal friction ϕ' [°] and dry unit weight γ'_d [kNm^{-3}] as function of relative density (expressed as a fraction in these correlations) (Lauder, 2010; Al-Defae, 2013):

$$\phi' = 20 \cdot I_d + 29 \tag{35}$$

$$\gamma'_d = 3 \cdot I_d + 14.5 \tag{36}$$

A plastic box was filled with dry sand to a height of 300 mm using pluviation. The plastic box was lined with 10 mm thick adhered wooden panels to provide walls that could easily be drilled for mounting roots. Internal dimensions were 530×330×310 mm (length×width×height). Roots were glued into pre-drilled holes, matching root analogue diameter, in the side of the box and supported by wires (cut prior to testing). Following analogue placement sand was pluviated into the box using a slot pluviator from a fixed height (Lauder, 2010; Al-Defae, 2013). Because roots were placed prior to pluviation, some shadowing might have occurred, potentially resulting in slightly lower densities directly under the root. Each box contained multiple roots positioned side by side. The main root axes were spaced at least 80 mm apart to prevent interference between tests, while branched roots were never buried next to each other.

3.3 Test equipment

The blade penetrometer shape was identical to that used by Meijer et al. (2016), i.e. a 30×2×38 mm (width × depth × height) plate welded to a standard agricultural penetrometer (12 mm diameter 30°

cone connected to a 10 mm diameter shaft) with a length of 500 mm. The agricultural penetrometer without a blade attached is referred to in the text as 'standard penetrometer'. Penetrometers were pushed down vertically using an universal testing machine (Instron 5980) fitted with a 30 kN load cell (Instron 2580 Static series, accurate to 0.5% of a reading down to 1/500th of the load cell capacity) with both force and displacement logged at 20 Hz. The test extension rate for the penetrometer was 300 mm min^{-1}, a value similar to the expected rates likely to be used in the field. 300 mm min^{-1} is also representative of landslide velocities and similar to previous testing (Meijer et al., 2016).

For reference testing, 10 blade and 11 standard penetrometer tests were performed in non-rooted ('fallow'), 50% relative density sand. In $I_d = 80\%$ non-rooted sand, 14 and 8 tests were performed respectively.

3.4 Data processing

In each depth–blade penetrometer resistance trace, soil and root effects were superimposed and there was some experimental variability in soil resistance. Root effects were isolated first by calculating the mean soil resistance without root effects at each depth level, resulting in a single 'average' fallow trace for each relative density. Subsequently, for each test the average ratio between the resistance measured during the test and the average fallow resistance was determined over a depth range $100 \leq z \leq 140$ mm (i.e. over the depth range just before the penetrometer encountered the buried root analogue). The root effect ('reinforcement') was then found by subtracting the product of this ratio and the average fallow resistance from the resistance trace measured in each test.

Reinforcement was only studied until the root broke, visible in the force–displacement diagram as a sudden decrease in penetrometer resistance (root peak resistance F_u). Additional peaks were visible over a displacement range of 0–40 mm following failure. Peaks evident following failure may be attributed to stick–slip, broken root ends sliding along the blade, and by broken root ends getting stuck behind the shoulder of the cone. These additional peaks were therefore discarded.

Exact root depth was required for accurate determination of the root peak displacement. Root depths were never exactly 150 mm due to experimental variation introduced during sample preparation. The depth could not be determined from the displacement–reinforcement plot due to increased resistance prior to touching the actual root. Both uniaxial tensile tests and 3-point bending tests showed highest root analogue stiffnesses at zero strain. Assuming this was also the case during blade penetrometer testing, for every test the magnitude and location of the largest gradient on the measured depth–root resistance curve was determined. Subsequently, the 'real' initial root depth was defined as the depth at which the the tangent at this location intersects the depth axis (Figure 10).

All data processing and statistical analyses were performed using R statistical software (R Core Team, 2013). Statistical significance of p-values is denoted as: $p = 0 < {}^{***} \leq 0.001 < {}^{**} \leq 0.01 < {}^{*} \leq 0.05 < {}^{\cdot} \leq 0.1 < {}^{n.s.}$

3.5 Predictions for forces and displacements

Predictions of root peak resistance and displacement were made using both the numerical and both analytical models. All models used the strength/stiffness fits (Figure 7) to account for variability introduced by root diameter. In the analytical cable model, ABS tensile parameters were used whereas in the analytical bending model bending parameters were used. Numerical modelling was performed separately for both bending and tensile parameters. In the numerical model, soil–root interface friction was modelled assuming Equation 6 (Case A). For all models, predictions were only made for horizontal roots due to model limitations. Predictions for inclined roots were made instead by assuming they were horizontally oriented. Since both analytical models assume infinitely long unbranched roots, no separate analytical model predictions could be made for roots with various lengths, loading positions and branching patterns.

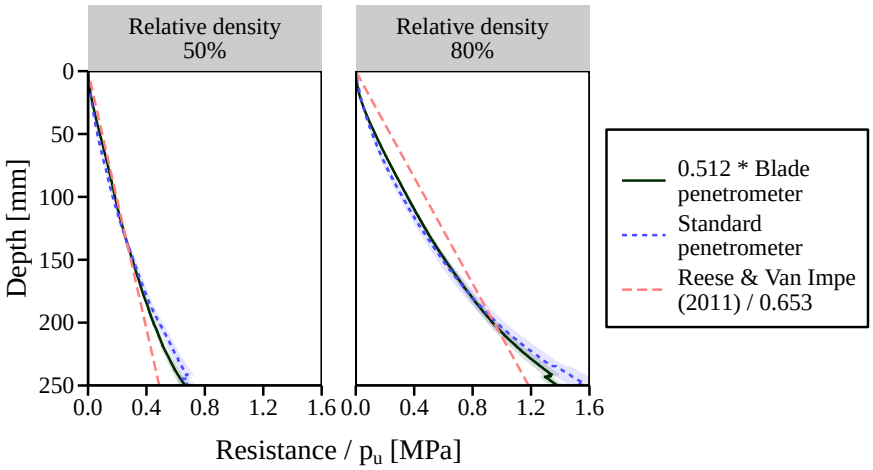

Figure 9: Average soil resistance over depth measured using the standard penetrometer and blade penetrometer (for both, resistances are calculated assuming load is distributed over the tip area of the standard penetrometer) and predicted using the model described by Reese and Van Impe (2011). Shaded areas indicate the standard error of the mean for experimentally measured results. Note the linear scaling factors for the measured blade penetrometer resistance (0.512) and the resistance predicted using Reese and Van Impe's model (1/0.653) to make them coincide with the experimentally measured standard penetrometer cone resistance.

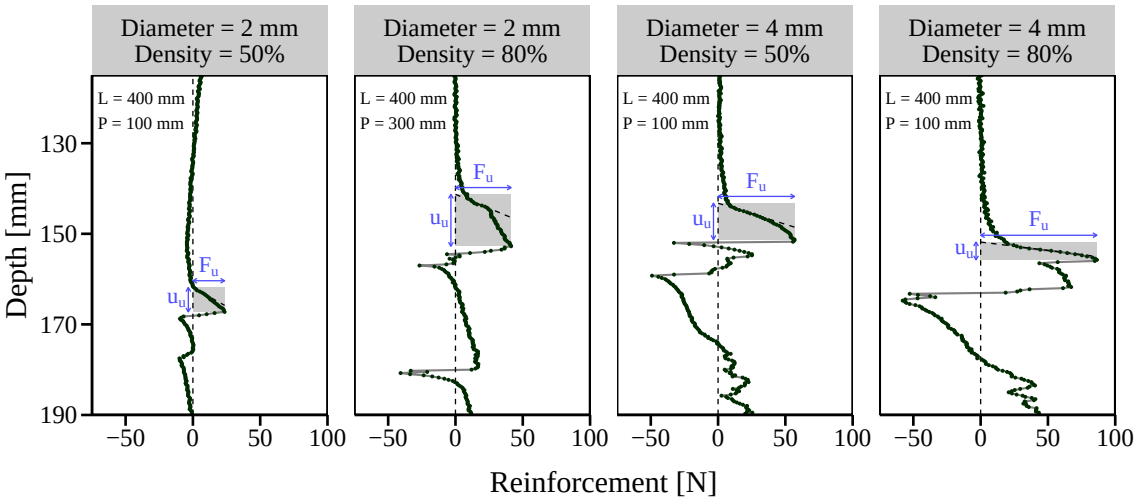

Figure 10: Example root resistance versus depth traces for horizontal roots. L indicates root length and P the distance between the trunk and the point of loading. F_u and u_u indicate the root peak resistance and root peak displacement respectively.

4 Validation of interpretative models

Standard cone penetrometer resistance, in non-rooted samples, was approximately half (0.497) of that recorded for the blade penetrometer (Figure 9), with a surface area only 24% smaller when compared to the blade penetrometer. This suggests shape effects and/or frictional resistance on the sides of the blade played a role. Predictions for soil resistance using Equation 5 yielded on average 37.7% lower resistances than measured using the standard penetrometer, when averaged between $z = 50$ mm (to avoid near-surface effects) and $z = 250$ mm (to avoid bottom boundary effects).

Figure 10 shows example root resistance–depth traces, showing the same type of clearly defined root reinforcement peaks as observed by Meijer et al. (2016). Measured root peak resistance increased with

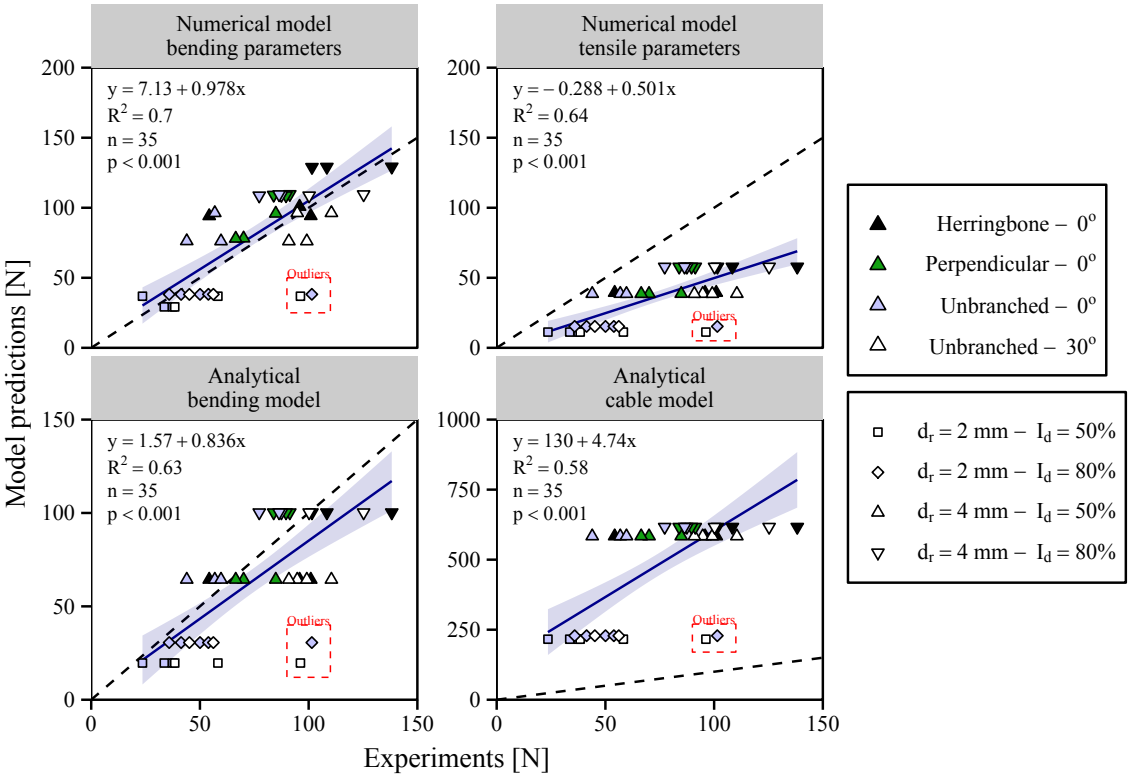

Figure 11: Comparison between experimentally measured and predicted root peak resistance values for varying root branching patterns, root inclination, root diameter and soil relative density. Solid lines indicate best linear fits, shaded areas the 95% confidence interval of the fit and the dashed line parity. Identified outliers, not taken into account in the fit, are indicated by a red box (both cases involved large resistances, possibly associated with a reduced soil resistance or shear failure, discussed in text).

increasing root diameter and soil density (Figures 10–11). Branching increased resistance compared to unbranched roots, with the herringbone type yielding approximately 23% higher reinforcements than perpendicular branching. When comparing roots with different lengths and loading positions, tests with 400 mm long roots loaded at 100 mm distance from the fixed point generally gave the highest results, although the effect of length and loading position was small in comparison.

The analytical cable model overestimated predictions of root peak resistance while the analytical bending model results closely resembled experimentally measured peak resistances. Highest coefficients of variation were observed in the analytical bending model ($R^2 = 0.7$), indicating ABS rods are likely to have failed in a bending rather than tension failure mechanism. Numerical simulation results also indicated that using bending parameters resulted in much better predictions than using tensile parameters.

Two outliers were observed in some of the tests on 400 mm long 2 mm diameter roots loaded at 100 mm distance from the fixed point. Both had much higher root peak resistances (101.5 and 96.2 N) and displacements (19.1 and 17.2 mm) compared to repeat tests. It is hypothesized that this was the result of variation in sample preparation. The density below the root might have been lower due to the root shadowing the area just below the root from pluviated sand, resulting in lower densities. This explains the higher displacements. Since the soil resistance is lower, a larger length of the root will displace, increasing the peak force. Because of the proximity of the 'parent root', the root will also be (partially) loaded in shear instead of bending, enhancing the higher resistances. Alternatively the differences could have been caused by variation in the mechanical properties or diameter introduced by the printing process.

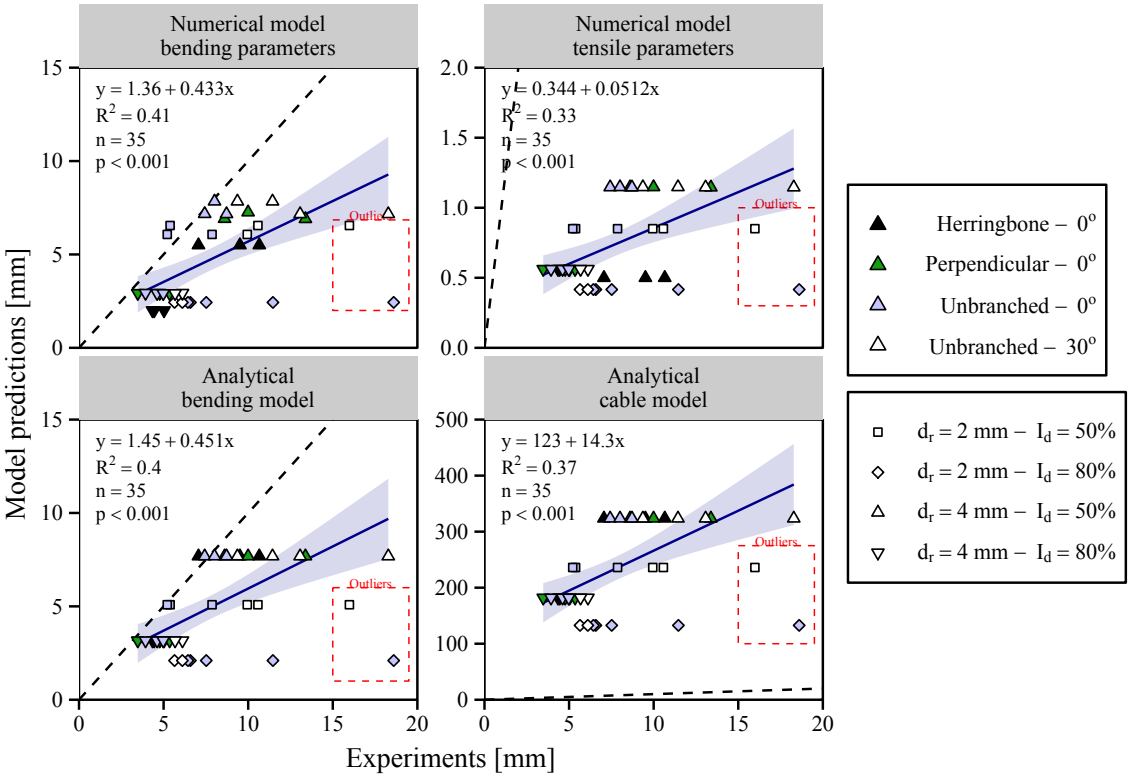

Figure 12: Comparison between experimentally measured and predicted root peak displacement for varying root branching patterns, root inclination, root diameter and soil relative density. Solid lines indicate best linear fits, shaded areas the 95% confidence interval of this fit and the dashed line parity. Identified outliers, not taken into account in the fit, are indicated by a red box.

Inclined root analogues (30°) resulted in higher root peak resistances (0–100%) compared to their horizontal counterparts, especially for thicker roots and those in lower density soils. These dependencies suggest that the failure mechanism might be different from the failure mechanism for horizontal roots. It is suggested that future work focusses on studying this effect and on development of better predictive models taking root inclination into account.

Perpendicular branching resulted in an increase in root peak resistance, but this increase was smaller than for herringbone branching. This is probably caused by the distance between branches and the loading point. Herringbone branches were located directly below the loading point and therefore strained more. Perpendicular branches were located further from the loading point, reducing strain. This distance also explains why in dense soil ($I_d = 80\%$) there was almost no difference in peak resistance between perpendicularly branched roots and unbranched roots, as due to the higher soil resistance, branches might have been too far away from the point of loading to be mobilised.

Inclined roots required larger displacements to reach failure than horizontal roots (Figure 12). Both root diameter and branching pattern had a small influence on the root peak displacement. The analytical bending model and numerical model using bending parameters yielded the best predictions and the best fits between experimentally measured and predicted root peak displacement (u_u). However, predictions were lower than displacements measured, and the variability in predictions was higher than those for peak resistance F_u ($R^2 = 0.40$–0.41 for u_u compared to 0.63–0.70 for F_u). This suggests large variation in experimental results or inaccuracies in the models.

Higher soil densities generally resulted in shorter root peak displacements, although 2 mm diameter roots in dense sand displaced much further compared with other roots even though peak resistances were similar. It is unclear what caused this effect. Reinforcement–depth traces (Figure 10) suggest

Table 2: Comparison of the magnitude of the root peak resistance for various factors. 'Data subset' indicates which experimental results were taken into account for deriving the mean and standard deviation ('SD') of the differences. The statistical significance was determined using paired t-tests.

Factor	Comparing			Data subset	Increase in root resistance			n
					Mean [%]	SD [%]	Significance [-]	[-]
Diameter	4 mm	vs.	2 mm	Horizontal & Unbranched	72.2	48.1	**	6
Relative density	80%	vs.	50%	Horizontal & Unbranched	74.7	81.8	*	6
Branching	Herringbone	vs.	Unbranched	Horizontal & $d_r = 4$ mm	50.8	47.6	*	6
	Perpendicular	vs.	Unbranched	Horizontal & $d_r = 4$ mm	23.0	25.5	·	6
Angle	30°	vs.	0°	Unbranched	47.2	49.1	**	8
Distance to trunk	100 mm	vs.	300 mm	Horizontal & Length = 400 mm	25.0	41.7	·	8
Length	400 mm	vs.	200 mm	Horizontal & Distance to trunk = 100 mm	16.4	32.6	$^{n.s.}$	8

a more gradual, plastic failure mechanism might have occurred. When these measurements were ignored, both the analytical bending model and numerical model using bending parameters resulted in decent predictions, although lower than measured. This is attributed to roots being modelled using a linear-elastic material using the secant stiffness at 90% strength. Since these models ignore any plastic deformation, the modelled strain to failure and therefore the predicted displacements will be lower.

Since predictions for root peak resistance values were better predicted than displacements, variability in root resistances was further analysed. Replicated tests for combinations of branching, diameter, inclination, relative density, length and loading position values were averaged so that a balanced selection of test results was obtained. The effect of various factors (e.g. root diameter, branching type etc.) was studied by pairwise comparison using two-sided Welch's t-test. For example, when quantifying the influence of root diameter, with the same inclination, branching, length, distance to trunk and relative density but different diameters were compared. The results (Table 2) showed that the variation in diameter and relative density had the strongest effects on the magnitude of the root peak resistance. Root branching and inclination had a lesser effect, while the effect of distance to trunk and especially root length was small. In addition, a type III analysis of variance test (ANOVA) was performed on the same dataset using the same factors. This analysis suggested that most of the variation in the data is explained by variation in root diameter (39%***), followed by relative density (14%***), root inclination (12%***), branching (11%**) and the distance to the trunk (5%**). Root length was non-significant(1%$^{n.s.}$). The importance of factors on the measured variation in root peak resistance as determined using the ANOVA roughly corresponds with that found using t-tests.

5 Implications for practical use

5.1 Simplification of p-y curves

Both the analytical bending and cable model assume that the full soil resistance is mobilised after infinitely small lateral root displacements instead of gradually, i.e.:

$$\begin{cases} p = 0 & \text{when } |u| = 0 \\ p = p_u & \text{when } |u| > 0 \end{cases} \tag{37}$$

Based on p-y theory (Reese and Van Impe, 2011) however, the soil reaches its maximum resistance after $3/80 \cdot d_r$. The effect of this simplification was studied by comparing numerical model simulations using both the full p-y curves (Figure 1) and the simplified approach using a rigid plastic model (Equation 37). Soil and root parameters were based on the experimental laboratory test conditions adopted. Results were compared for 2 and 4 mm diameter ABS rods in dry sand with relative densities between 10 and 90%. The root depth was varied between 50, 100, 200 and 500 mm to model a wide range of conditions. The root length was set to 250 mm to both sides of the penetrometer and all degrees of freedom were restrained at root ends.

The difference between results obtained with the simplified p_u approach or full modelling of the p-y curve was considered to be related to the ratio of lateral displacement at which the full curve reaches its maximum resistance ($y_u = 3/80 \cdot d_r$) and the root peak displacement at root failure (u_u). Using Table 1, this ratio is proportionate to $p_u \cdot E \cdot \sigma^{-2}$. The smaller this ratio, the less effect the differences in p-y behaviour between $0 \leq u \leq y_u$ would be expected to have on the root reinforcement peaks.

The simplified approach almost yielded the same results as obtained by modelling the full p-y curve, especially for the root peak resistance (Figure 13). The accuracy decreases with increasing root bending and soil stiffness and with decreasing root strengths. For the worst case in the laboratory testing programme ($d_r = 4$ mm, $p_u \approx 0.5$ MPa) the peak force is only 0.8% higher and the displacement 3.3% lower by using the simplified approach compared to modelling the full p-y curve. Because the roots displace large distances compared to the displacement required to reach the full soil resistance, the simplified soil resistance approach was considered valid for the experimental conditions tested.

5.2 Limitations on the use of the analytical models

The analytical bending yielded good predictions for the experimentally measured root peak resistance, but was dependent on many model assumptions, e.g. neglecting non-linear geometric effects. To study when this model yielded accurate results numerical simulations were performed. First it was investigated in which cases roots are primarily loaded in bending. Parameters which are varied were the distance to the constraint on either side ($L \in \{0.5, 1, 2, 4, 8\} \times L_{crit}$), root strength ($\sigma \in \{2, 5, 10, 20, 50, 100\}$ MPa), root Young's modulus ($E \in \{100, 200, 500, 1000, 2000\}$ MPa) and ultimate soil resistance ($p_u \in \{0.1, 0.2, 0.5, 1, 2\}$ MPa). Two different models were run. In the first, axial constraints were high (axial deformation prevented at root tips + high root–soil interface friction case ($\tau_i \approx p/\pi \cdot \cos\beta$)), while in the second no axial constraints were modelled (axial deformation possible at root ends + no root–soil interface friction ($\tau_i \approx 0$)). In the latter case, a smaller number of parameter combinations was adopted to minimise the numerical workload. Soil springs were modelled using the simplified curves (Equation 37).

Comparison between the numerical simulations showed that the analytical bending solution gives similar results to the analytical bending model when (Figure 14):

$$\frac{u_u}{L_{crit}} \leq 0.05 \tag{38}$$

or in terms of soil and root parameters:

$$\frac{\sigma_b^{1.5}}{p_u^{0.5} \cdot E_b} \leq 0.424 \tag{39}$$

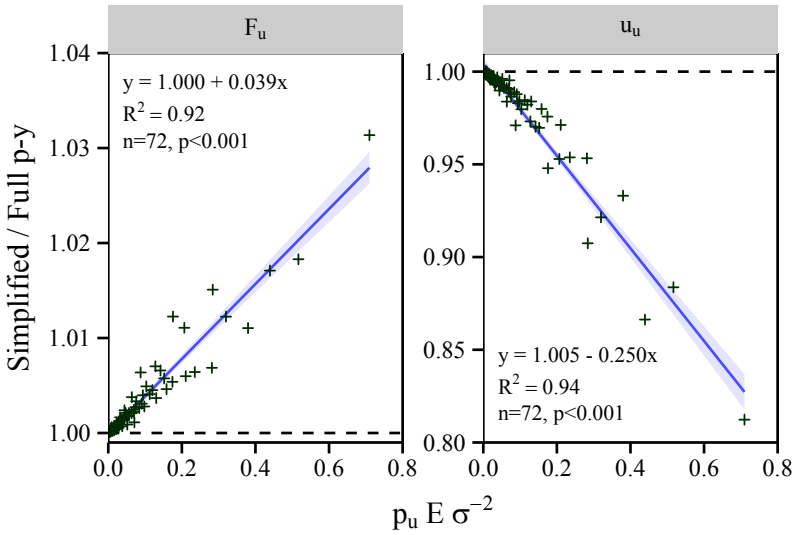

Figure 13: Comparison between numerical simulations simulating the full *p-y* curve or the simplified approach. a) root peak resistance (F_u), b) effect on root peak displacement (u_u). $p_u\ E\ \sigma^{-2}$ indicates the ratio between the displacement required to reach the full soil resistance (according to *p-y* theory by Reese and Van Impe (2011)) and u_u, expressed in terms of root and soil properties, see text. $p_u \cdot E \cdot \sigma^{-2}$ ranges between 0.04 and 0.15 in the laboratory experiments. The shaded area indicates the 95% confidence interval of the fit.

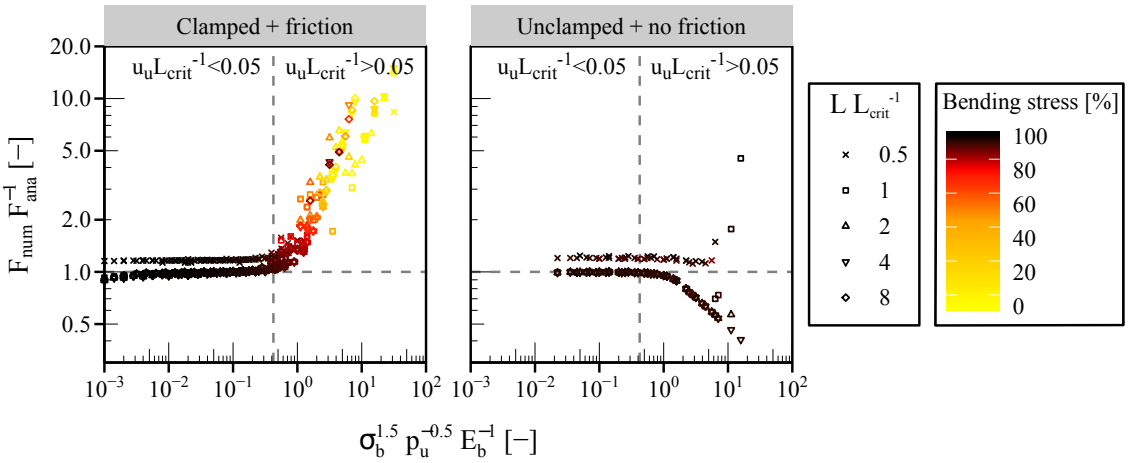

Figure 14: Comparison for simulated root peak resistance between predicted numerical (F_{num}) and analytical beam (F_{ana}) models for various root parameters, soil resistances and soil–root interface friction assumptions.

When the root is axially constrained, when $\sigma_b^{1.5} \cdot p_u^{-0.5} \cdot E_b^{-1} > 0.424$ predicted root peak resistances were higher and a smaller proportion of the root stress was caused by bending effects, indicating a build-up of tensile forces. In the unconstrained case, the resistance is less sensitive to changes in the dimensionless parameter group $\sigma_b^{1.5} \cdot p_u^{-0.5} \cdot E_b^{-1}$. In both cases, the ratio between numerical and analytical bending model forces is relatively independent from the length of the root, given that $L \geq L_{crit}$.

The analytical bending model predictions for root peak resistance were close to the experimentally measured values, suggesting the ABS root analogues failed in bending. The highest value for $\sigma_b^{1.5} \cdot p_u^{-0.5} \cdot E_b^{-1}$ equals approximately 0.80 ($I_d = 50\%$, $d_r = 2$ mm) and the lowest 0.48 ($I_d = 80\%$, $d_r = 4$ mm). These values are just above the identified threshold level of 0.424, derived from numerical modelling

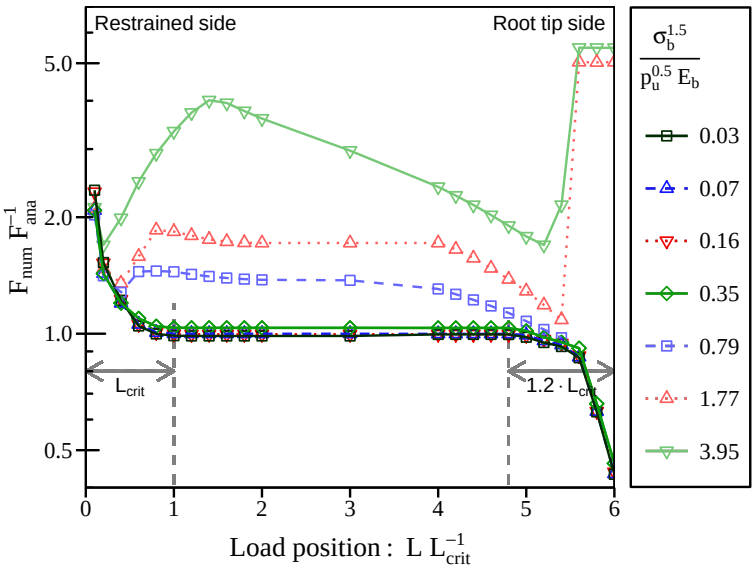

Figure 15: Comparison for simulated root peak resistance between predicted numerical (F_{num}) and analytical beam (F_{ana}) for various root and soil parameters and distances to a root boundary.

(Equation 39), below which numerical and analytical bending models yielded the same results for F_u. This explained why the numerical bending model yielded similar but slightly higher predictions than the analytical bending model. Secondly, the magnitude of this dimensionless group of parameters explains why the root analogues failed largely due to bending rather than tension mechanisms (Figure 14).

The analytical bending model assumes infinitely long roots. However, in reality roots might be loaded close to a root tip or close to the trunk or parent root. The behaviour of roots loaded close to a boundary was investigated using the numerical model as in practice a penetrometer test may be conducted close to the root anchorage, close to the tip, or anywhere in between (the root length is not known a priori). A root with length $6 \cdot L_{crit}$ was modelled. The left end was fully restrained (parent root) and the right end unsupported (root end). The distance between the point of loading and either boundary was varied between 0 and $2 \cdot L_{crit}$ in steps of $0.2 \cdot L_{crit}$ for various root and soil properties ($d_r \in \{2, 10\}$ mm; $\sigma \in \{10, 50\}$ MPa; $E \in \{200, 1000\}$ MPa, $p_u \in \{0.2, 1\}$ MPa).

When Equation 39 is met, Figure 15 shows that the analytical bending method is accurate so long as the penetrometer test is not carried out within $1.2 \cdot L_{crit}$ of the ends of the root. In the experiments conducted, predicted values for L_{crit} ranged between 26.8 and 68.4 mm while the minimum distance to the trunk or root tip is 100 mm, fulfilling this condition. When an error of approximately 10% is deemed acceptable, the analytical bending solution is valid when the root is loaded at least approximately $0.5 \cdot L_{crit}$ from either end. I

5.3 Accuracy of root diameter predictions

Practical application of the modified ('blade') penetrometer (see Meijer et al., 2017) characterisation of root peaks identified in the measured depth–resistance trace may be used to back-analyse the root diameter. Rewriting the analytical bending model equation (point load, Table 1) to find root diameter based on the measured root peak resistance (d_p) yields:

$$d_p = 0.9886 \cdot F_u^{0.5} \cdot \sigma_b^{-0.25} \cdot p_u^{0.25} \tag{40}$$

This shows that the diameter prediction is less sensitive to changes in root strength and soil resistance compared to changes in measured root peak resistance. When the equation for root peak displacement

(analytical bending model) is rewritten:

$$d_p = 10.20 \cdot u_u \cdot \sigma_b^{-2} \cdot E_b \cdot p_u \tag{41}$$

Comparing to Equation 40 indicates that predictions based on root peak displacement are likely to be less accurate. Small variations in root stiffness, soil resistance and especially root strength will have large effects on the predicted diameter compared to the effect of variation in the measured displacement at peak force. This explained why the experimentally measured root peak resistance could be predicted much more accurately than the accompanying displacements when using the analytical bending model.

Similar dependencies were found for the analytical cable model. When the root diameter is predicted based on the root peak resistance and assuming $\zeta = 0.5$, a 100% increase in F_u results in an increase in d_p of 41%. A 100% increase in σ_t or p_u reduces F_u by 31 or 3% respectively, while a similar increase in E_t or τ_i yield an increase of only 4%. When the diameter is predicted based on u_u, d_p is changed by +100% (u_u), -64% (σ_t) or +41% (E_t, p_u or τ_i) when these parameters are increased by 100%. Again, the prediction based on root peak resistance measurement is less sensitive to changes in root strength, root stiffness, soil resistance or root–soil interface friction, compared with predictions based on the root peak displacement.

5.4 Suggested field use

The variation in experimental root peak resistance results was best explained by variations in root diameter and soil relative density. Branching and root inclination were of limited importance, while the effects of root loading distance and root length were even less so. Results explained why the analytical bending model resulted in reliable predictions for the peak resistance for horizontal root analogues despite ignoring root length, branching and distance to trunk.

The few parameters required for both analytical models makes them easy to use in practical applications and minimises the need for time-consuming numerical modelling. Both analytical models require estimates for root strength and stiffness. Biomechanical data can be easily acquired using standard material testing (tensile and bending tests), and for many species tensile data has been published before although data on root stiffness is sparse (e.g. Mao et al., 2012) and data on bending properties almost non-existent. A third required parameter, soil resistance p_u, can be estimated for dry sand when soil properties (ϕ' and γ') are known using Equation 5. For the practical application of this method, it might be easier to estimate p_u from standard penetrometer testing or even from blade penetrometer testing (see Meijer et al., 2017). This study showed that in this case correction factors are required to compensate for the difference in shape between the penetrometer and the root. The cable model requires an additional value for root–soil interface friction (τ_i). In field conditions, this value could be estimated in principle on the basis of measuring soil–soil shear strength (e.g. from in situ shear tests such as vane testing or from penetrometer resistance when penetrometer resistance–shear strength correlations are available) and applying a correction factor to obtain the soil–root friction.

5.5 Comparison with existing models

The analyses showed that modelling soil resistance on laterally displacing roots is better modelled using a constant soil resistance (similar to Wu, 2007, 2013) instead of linear springs (Wu et al., 1988). This approach is consistent with the experimentally verified *p-y* theory on laterally loaded piles displaced by relatively large distances compared to pile diameter. The simple analytical bending model solutions provide a practical and simple model to estimate the resistance and displacements of loaded roots when root mechanical properties and soil resistances are known. However, root displacements in experiments were still significantly greater than analytical bending model predictions. This is attributed to the analytical model not being able to take plastic root analogue deformation into account.

The analytical cable model is an improvement compared to existing cable models (e.g. Wu et al., 1988; Wu, 2007, 2013) because of its ability to take non-linear deformation effects and axial elongation

into account. However, since root analogues in the experiments described here were relatively stiff and failed in bending, cable model predictions were inaccurate. Because many real roots are more flexible than ABS analogues (Meijer et al., 2016), the analytical cable model is expected to yield better predictions than the bending model for many real root cases.

6 Conclusions

- Several interpretative models were developed to predict the behaviour of a root loaded by a point load, based on root strength, root stiffness and soil resistance. Developed models can also be used to predict the resistance and corresponding displacements of roots crossing a shear plane. The incorporation of root elasticity and soil resistance and the ability to estimate displacements as well as resistances provide major improvements over the traditional Wu/Waldron model solution for single roots.

- Numerical model simulations show that the gradual mobilisation of soil resistance against lateral root displacement can be neglected because root displacements are large compared to the displacement required to mobilise the full soil resistance. This allows for simply using the ultimate soil resistance (p_u) in models.

- The simple analytical bending model yields comparable results to numerical models when the root displacements are relatively small, i.e. when the root strength is weak and root stiffness and soil resistance large, and when the root is not loaded close to a root boundary (root tip or parent root).

- Experimental penetrometer results for buried ABS root analogues in dry sand show that the force required to break horizontal root analogues is mainly a function of root diameter. The second most important parameter is soil density/strength. Root branching, length and the position of loading all have a smaller influence.

- The force required by a penetrometer to fail an ABS root analogue was best predicted using the numerical model (using strength and stiffness parameters derived from 3-point bending tests) or the analytical bending model, showing that the root analogues failed in bending rather than tension.

- All models poorly predict penetrometer displacement required to reach root failure.

- Root inclination potentially has a strong effect on both root peak resistance and displacement. However, the experimental results could not be compared to modelling predictions because of model limitations. This effect should be addressed during further model development.

- Root diameters can be predicted from 'root peaks' identified in the penetrometer force–depth trace when root mechanical properties and soil resistance are known or accurately estimated if the correct root failure mechanism (bending or tension) is known. Predictions based on the root peak resistance F_u are more reliable than those based on lateral root displacement to reach peak force u_u.

- Both the root diameters and root location (location and depths) are essential pieces of information required when mechanical root-reinforcement is to be quantified. Both are measured by the blade penetrometer and can easily be implemented into existing root-reinforcement models.

- A follow-up paper (Meijer et al., 2017) will apply and further validate these methods against field data collected for two contrasting sites/species. This will yield data for more realistic soil (real field soil instead of dry sand) and root conditions (real plant roots instead of ABS root analogues).

Acknowledgements

G. J. Meijer acknowledges a studentship provided by Forest Research and funded by ClimateXChange, the Scottish Government's Centre for Expertise on Climate Change. The James Hutton Institute receives funding from the Scottish Government. The authors thank the manuscript reviewers for their helpful comments.

Notation

A - Soil cross-sectional area [mm^2]
A_r - Root cross-sectional area [mm^2]
$\overline{A}_s$ - Model constant in p-y model by Reese and Van Impe (2011)
c_r - Root cohesion [kPa]
d_r - Root diameter [mm]
d_p - Predicted root diameter [mm]
E - Secant stiffness at 90% of peak strength [MPa]
E_b - Secant bending stiffness at 90% of peak bending strength [MPa]
E_t - Secant tensile stiffness at 90% of peak tensile strength [MPa]
F - Penetrometer resistance [N]
F_u - Root peak resistance, i.e. maximum increase in penetrometer resistance due to a root [N]
F_t - Root tensile force at failure [N]
I - Second moment of area [mm^4]
I_d - Soil relative density [%]
K_0 - Coefficient of lateral earth pressure at rest [-]
K_a - Coefficient of lateral earth pressure (active) [-]
k - Spring stiffness [Nmm^{-1}]
k' - Ratio between root cohesion and total root tensile strength [-]
k'' - Reduction factor calculation of c_r due to root sequential breakage [-]
L - Root length [mm]
L_1 - Length of laterally displaced root in analytical bending model [mm]
L_2 - Length of laterally displaced root in analytical bending model [mm]
L_{arc} - Arc length of a parabolic section [mm]
L_{crit} - Length of the zone of lateral root displacement on either side of loading [mm]
L_I - Length of laterally displaced root in analytical cable model [mm]
L_{II} - Length of axially displaced root in analytical cable model [mm]
M - Bending moment [Nmm]
M_u - Bending moment at root failure [Nmm]
n - Number of samples tested [-]
P - Loading position (distance to parent root/container wall) along the root axis [mm]
p - Soil resistance against lateral root displacement [MPa]
p - Statistical significance [-]
p_u - Ultimate soil resistance against lateral root displacement [MPa]
RAR - Root area ratio [-]
T_x - Axial root force [N]
u - Root lateral displacement [mm]
u_u - Root peak displacement, i.e. root lateral displacement at root failure [mm]
z - Root depth [mm]
α - Ratio of displacing root lengths in analytical bending model [-]
β - Angle between root axis and direction perpendicular to the direction of loading [°]
γ - Soil unit weight [kNm^{-3}]
ζ - Dimensionless parameter in analytical cable model [-]

η - Dimensionless parameter in analytical cable model [-]
σ - Peak strength [MPa]
σ_b - Peak strength in bending [MPa]
σ_t - Peak strength in uniaxial tension [MPa]
τ_i - Root–soil interface friction [kPa]
ϕ' - Soil angle of internal friction [°]

References

Ehsan Abdi, Baris Majnounian, Maria Genet, and Hassan Rahimi. Quantifying the effects of root reinforcement of Persian ironwood (*Parrotia persica*) on slope stability; a case study: Hillslope of Hyrcanian forests, northern Iran. *Ecological Engineering*, 36(10):1409–1416, 2010.

B. Abernethy and I. D. Rutherfurd. The distribution and strength of riparian tree roots in relation to riverbank reinforcement. *Hydrological Processes*, 15(1):63–79, 2001.

D. L. Achat, M. R. Bakker, and P. Trichet. Rooting patterns and fine root biomass of *Pinus pinaster* assessed by trench wall and core methods. *Journal of Forest Research*, 13(3):165–175, 2008.

Alexis Achim and Bruce C. Nicoll. Modelling the anchorage of shallow-rooted trees. *Forestry*, 82(3): 273–284, 2009.

A. H. Al-Defae. *Seismic performance of pile-reinforced slopes.* PhD thesis, University of Dundee, 2013.

American Petroleum Institute. *Recommended practice for planning, desdesign and constructing fixed offshore platforms – Working stress design: API recommended practice 2A-WSD, 21st edition, December 2000. Errata and supplement 1, December 2002.* American Petroleum Institute, 2000.

C. Ammer and S. Wagner. An approach for modelling the mean fine-root biomass of Norway spruce stands. *Trees – Structure and Function*, 19(2):145–153, 2005.

A. G. Bengough and C. E. Mullins. Mechanical impedance to root growth: a review of experimental techniques and root growth responses. *Journal of Soil Science*, 41(3):341–358, 1990.

A. G. Bengough, C. J. Mackenzie, and A. J. Diggle. Relations between root length densities and root intersections with horizontal and vertical planes using root growth modelling in 3-dimensions. *Plant and Soil*, 145(2):245–252, 1992.

Gian Battista Bischetti, Enrico Antonio Chiaradia, Thomas Epis, and Emanuele Morlotti. Root cohesion of forest species in the Italian Alps. *Plant and Soil*, 324(1-2):71–89, 2009.

Isabella Børja, Heleen A. De Wit, Arne Steffenrem, and Hooshang Majdi. Stand age and fine root biomass, distribution and morphology in a Norway spruce chronosequence in southeast Norway. *Tree Physiology*, 28(5):773–784, 2008.

J. Brisson and J. F. Reynolds. The effect of neighbors on root distribution in a creosotebush (*Larrea tridentata*) population. *Ecology*, 75(6):1693–1702, 1994.

B. B. Casper, H. J. Schenk, and R. B. Jackson. Defining a plant's belowground zone of influence. *Ecology*, 84(9):2313–2321, 2003.

N. Coppin and I. Richards. *Use of vegetation in civil engineering, CIRIA book 10.* Butterworths, Kent, 1990.

M. P. Coutts. Root architecture and tree stability. *Plant and Soil*, 71(1–3):171–188, 1983.

M. P. Coutts and B. C. Nicoll. Orientation of the lateral roots of trees .1. upward growth of surface roots and deflection near the soil surface. *New Phytologist*, 119(2):227–234, 1991.

F. Danjon, D. Bert, A. Porté, C. Meredieu, P. Trichet, F. Lagane, and B. Issenhuth. Effect of fertilization on 3D root architecture in 12-year-old *Pinus pinaster* trees. In *Proceedings 4th International Symposium on Dynamics of Physiological Processes in Roots of Woody Plants, 16th–19th September 2007, Bangor, UK*, page 36, 2007.

F. Danjon, D. H. Barker, M. Drexhage, and A. Stokes. Using three-dimensional plant root architecture in models of shallow-slope stability. *Annals of Botany*, 101(8):1281–1293, 2008.

A. Di Iorio, B. Lasserre, G. S. Scippa, and D. Chiatante. Root system architecture of *Quercus pubescens* trees growing on different sloping conditions. *Annals of Botany*, 95(2):351–361, 2005.

B. B. Docker and T. C. T. Hubble. Modelling the distribution of enhanced soil shear strength beneath riparian trees of south-eastern Australia. *Ecological Engineering*, 35(5):921–934, 2009.

N. R. Duckett. *Development of improved predictive tools for mechanical soil root interaction.* PhD thesis, University of Dundee, 2014.

L. Dupuy, T. Fourcaud, and A. Stokes. A numerical investigation into factors affecting the anchorage of roots in tension. *European Journal of Soil Science*, 56(3):319–327, 2005a.

L. Dupuy, T. Fourcaud, and A. Stokes. A numerical investigation into the influence of soil type and root architecture on tree anchorage. *Plant and Soil*, 278(1–2):119–134, 2005b.

Marie Genet, Nomessi Kokutse, Alexia Stokes, Thierry Fourcaud, Xiaohu Cai, Jinnan Ji, and Slobodan Mickovski. Root reinforcement in plantations of *Cryptomeria japonica* D. Don: effect of tree age and stand structure on slope stability. *Forest Ecology and Management*, 256(8):1517–1526, 2008.

F. Giadrossich, M. Schwarz, D. Cohen, F. Preti, and D. Or. Mechanical interactions between neighbouring roots during pullout tests. *Plant and Soil*, 367(1–2):391–406, 2013.

Donald H. Gray and Robbin B. Sotir. *Biotechnical and soil bioengineering slope stabilization, a practical guide for erosion control.* John Wiley & Sons Inc, New York, 1996.

O. Hamza, A. G. Bengough, M. F. Bransby, M. C. R. Davies, and P. D. Hallett. Mechanics of root-pullout from soil: a novel image and stress analysis procedure. In A. Stokes, I. Spanos, J. E. Norris, and E. Cammeraat, editors, *Eco- and ground bio-engineering: the use of vegetation to improve slope stability*, pages 13–20. Springer, Dordrecht, The Netherlands, 2007.

R. Henderson, E. D. Ford, and E. Renshaw. Morphology of the structural root-system of Sitka spruce. 2. computer-simulation of rooting patterns. *Forestry*, 56(2):137–153, 1983a.

R. Henderson, E. D. Ford, E. Renshaw, and J. D. Deans. Morphology of the structural root-system of Sitka spruce: 1. analysis and quantitative description. *Forestry*, 56(2):121–135, 1983b.

R. C. Hibbeler. *Structural analysis (9th edition).* Prentice Hall, Upper Saddle River, NJ, US, 2014.

Yasuhiro Hirano, Masako Dannoura, Kenji Aono, Tetsurou Igarashi, Masahiro Ishii, Keitarou Yamase, Naoki Makita, and Yoichi Kanazawa. Limiting factors in the detection of tree roots using ground-penetrating radar. *Plant and Soil*, 319(1–2):15–24, 2009.

B. John, H. N. Pandey, and R. S. Tripathi. Vertical distribution and seasonal changes of fine and coarse root mass in *Pinus kesiya* Royle ex. Gordon forest of three different ages. *Acta Oecologica*, 22(5–6):293–300, 2001.

K. Lauder. *The performance of pipeline ploughs.* PhD thesis, University of Dundee, 2010.

T. Liang and J. A. Knappett. Centrifuge modelling of the influence of slope height on the seismic performance of rooted slopes. *Géotechnique*, 2017. doi: http://dx.doi.org/10.1680/geot./16.P.072. In press.

T. Liang, J.A. Knappett, and A.G. Bengough. Scale modelling of plant root systems using 3-D printing. In Christophe Gaudin and David White, editors, *ICPMG2014 – Physical Modelling in Geotechnics*, volume 1, pages 361–366, Leiden, The Netherlands, 2014. CRC.

T. Liang, J.A. Knappett, and N. Duckett. Modelling the seismic performance of rooted slopes from individual root–soil interaction to global slope behaviour. *Géotechnique*, 65(12):995–1009, 2015.

Z. Mao, F. Bourrier, A. Stokes, and T. Fourcaud. Three-dimensional modelling of slope stability in heterogeneous montane forest ecosystems. *Ecological Modelling*, 273:11–22, 2014.

Zhun Mao, Laurent Saint-Andre, Marie Genet, Francois-Xavier Mine, Christophe Jourdan, Herve Rey, Benoit Courbaud, and Alexia Stokes. Engineering ecological protection against landslides in diverse mountain forests: Choosing cohesion models. *Ecological Engineering*, 45:55–69, 2012.

G. J. Meijer, A. G. Bengough, J. A. Knappett, K. W. Loades, and B. C.. Nicoll. New in-site techniques for measuring the properties of root-reinforced soil – laboratory evaluation. *Géotechnique*, 66(1): 27–40, 2016.

G. J. Meijer, A. G. Bengough, J. A. Knappett, K. W. Loades, and B. C.. Nicoll. In situ root identification through blade penetrometer testing – part 2: field testing. *Géotechnique*, 2017. In press.

S. B. Mickovski, A. G. Bengough, M. F. Bransby, M. C. R. Davies, P. D. Hallett, and R. Sonnenberg. Material stiffness, branching pattern and soil matric potential affect the pullout resistance of model root systems. *European Journal of Soil Science*, 58(6):1471–1481, 2007.

Christine Moos, Peter Bebi, Frank Graf, Josias Mattli, Christian Rickli, and Massimiliano Schwarz. How does forest structure affect root reinforcement and susceptibility to shallow landslides? *Earth Surface Processes and Landforms*, 41(7):951–960, 2016. doi: 10.1002/esp.3887.

B. C. Nicoll and D. Ray. Adaptive growth of tree root systems in response to wind action and site conditions. *Tree Physiology*, 16(11–12):891–898, 1996.

B. C. Nicoll, A. Achim, S. Mochan, and B. A. Gardiner. Does steep terrain influence tree stability? a field investigation. *Canadian Journal of Forest Research*, 35(10):2360–2367, 2005.

B. C. Nicoll, S. Berthier, A. Achim, K. Gouskou, F. Danjon, and L. P. H. van Beek. The architecture of *Picea sitchensis* structural root systems on horizontal and sloping terrain. *Trees – Structure and Function*, 20(6):701–712, 2006.

Joanne E. Norris, Alexia Stokes, Slobodan B. Mickovski, Eric Cammeraat, Rens Van Beek, Bruce C. Nicoll, and Alexis Achim. *Slope stability and erosion control: Ecotechnical solutions*. Springer, Dordrecht, The Netherlands, 2008.

V. Operstein and S. Frydman. The influence of vegetation on soil strength. *Ground Improvement*, 4: 81–89, 2000.

A. Pierret, C. J. Moran, C. B. McLachan, and J. M. Kirby. Measurement of root length density in intact samples using x-radiography and image analysis. *Image Analysis & Stereology*, 19(2):145–149, 2000.

N. Pollen and A. Simon. Estimating the mechanical effects of riparian vegetation on stream bank stability using a fiber bundle model. *Water Resources Research*, 41(7):W07025, 2005.

J. Puhe. Growth and development of the root system of norway spruce (*Picea abies*) in forest stands – a review. *Forest Ecology and Management*, 175(1–3):253–273, 2003.

R Core Team. *R: A Language and Environment for Statistical Computing*. R Foundation for Statistical Computing, Vienna, Austria, 2013. URL http://www.R-project.org/.

Mark Randolph and Susan Gourvenec. *Offshore geotechnical engineering*. Spon, New York, US, 2011.

Lymon C. Reese and William F. Van Impe. *Single piles and pile groups under lateral loading, 2nd edition*. CRC, Leiden, The Netherlands, 2011.

Mary M. Riestenberg. *Anchoring of thin colluvium by roots of sugar maple and white ash on hillslopes in Cincinnati, US Geological Survey Bulletin 2059-E*. US Government Print Office, Washington, US, 1994.

J. J. Roering, K. M. Schmidt, J. D. Stock, W. E. Dietrich, and D. R. Montgomery. Shallow landsliding, root reinforcement, and the spatial distribution of trees in the Oregon Coast Range. *Canadian Geotechnical Journal*, 40(2):237–253, 2003.

K. M. Schmidt, J. J. Roering, J. D. Stock, W. E. Dietrich, D. R. Montgomery, and T. Schaub. The variability of root cohesion as an influence on shallow landslide susceptibility in the Oregon Coast Range. *Canadian Geotechnical Journal*, 38(5):995–1024, 2001.

M. Schwarz, P. Lehmann, and D. Or. Quantifying lateral root reinforcement in steep slopes – from a bundle of roots to tree stands. *Earth Surface Processes and Landforms*, 35(3):354–367, 2010.

G. S. Scippa, M. Di Michele, A. Di Iorio, A. Costa, B. Lasserre, and D. Chiatante. The response of *Spartium junceum* roots to slope: Anchorage and gene factors. *Annals of Botany*, 97(5):857–866, 2006.

S. J. Steele, S. T. Gower, J. G. Vogel, and J. M. Norman. Root mass, net primary production and turnover in aspen, jack pine and black spruce forests in Saskatchewan and Manitoba, Canada. *Tree Physiology*, 17(8–9):577–587, 1997.

A. Stokes, T. Fourcaud, J. Hruska, J. Çermák, N. Nadyezdhina, V. Nadyezhdin, and L. Praus. An evaluation of different methods to investigate root system architecture of urban trees in situ: I. ground-penetrating radar. *Journal of Arboriculture*, 28(1):2–10, 2002.

Alexia Stokes, Murad Abd. Ghani, Franck Salin, Frédéric Danjon, Henri Jeannin, Stéphanie Berthier, Adzo Dzifa Kokutse, and Henri Frochot. Root morphology and strain distribution during tree failure on mountain slopes. In A. Stokes, I. Spanos, J. E. Norris, and E. Cammeraat, editors, *Eco- and ground bio-engineering: the use of vegetation to improve slope stability*, pages 165–173. Springer, 2007.

Alexia Stokes, Joanne E. Norris, L. P. H. Van Beek, Thom Bogaard, Erik Cammeraat, Sloban B. Mickovski, Anthony Jenner, Antonino Di Iorio, and Thierry Fourcaud. How vegetation reinforces soil on slopes. In J. E. Norris, A. Stokes, S. B. Mickovski, E. Cammeraat, R. Van Beek, B. C. Nicoll, and A. Achim, editors, *Slope stability and erosion control: Ecotechnological solutions*, pages 65–118. Springer, 2008.

Alexia Stokes, Claire Atger, Anthony Glyn Bengough, Thierry Fourcaud, and Roy C. Sidle. Desirable plant root traits for protecting natural and engineered slopes against landslides. *Plant and Soil*, 324 (1–2):1–30, 2009.

André Guy Tranquille Temgoua, Nomessi K. Kokutse, and Zanin Kavazović. Influence of forest stands and root morphologies on hillslope stability. *Ecological Engineering*, 95:622–634, 2016.

Matteo Tosi. Root tensile strength relationships and their slope stability implications of three shrub species in the northern Apennines (Italy). *Geomorphology*, 87(4):268–283, 2007.

S. Volis and U. Shani. The effect of neighbors on the root system of the desert annual *Eremobium aegyptiacum*. *Folia Geobotanica*, 35(2):161–168, 2000.

L. J. Waldron. Shear resistance of root-permeated homogeneous and stratified soil. *Soil Science Society of America Journal*, 41(5):843–849, 1977.

Zhengquan Wang, Dali Guo, Xiangrong Wang, Jiacun Gu, and Li Mei. Fine root architecture, morphology, and biomass of different branch orders of two Chinese temperate tree species. *Plant and Soil*, 288(1–2):155–171, 2006.

A. Watson, C. Phillips, and M. Marden. Root strength, growth, and rates of decay: root reinforcement changes of two tree species and their contribution to slope stability. *Plant and Soil*, 217(1–2):39–47, 1999.

T. H. Wu. *Root reinforcement: analyses and experiments*, volume 103 of *Eco- and Ground Bio-Engineering: The Use of Vegetation to Improve Slope Stability*. Springer, Dordrecht, 2007.

T. H. Wu, W. P. McKinnell III, and D. N. Swanston. Strength of tree roots and landslides on Prince of Wales Island, Alaska. *Canadian Geotechnical Journal*, 16(1):19–33, 1979.

T. H. Wu, R. M. McOmber, R. T. Erb, and P. E. Beal. Study of soil–root interaction. *Journal of Geotechnical Engineering (ASCE)*, 114(12):1351–1375, 1988.

Tien H. Wu. Root reinforcement of soil: review of analytical models, test results and applications to design. *Canadian Geotechnical Journal*, 50(3):259–274, 2013.